Infrared Metamaterial Absorbers: Fundamentals and Applications

Author: Xianliang Liu

Boston College

The Graduate School of Arts and Sciences

Department of Physics

INFRARED METAMATERIAL ABSORBERS: FUNDAMENTALS AND APPLICATIONS

A DISSERTATION

by

XIANLIANG LIU

submitted in partial fulfillment of the requirements

for the degree of

Doctor of Philosophy

June 2013

INFRARED METAMATERIAL ABSORBERS: FUNDAMENTALS AND APPLICATIONS

by

XIANLIANG LIU

Advisor: Willie J. Padilla

Abstract

Realization of an ideal electromagnetic absorber has long been a goal of engineers and is highly desired for frequencies above the microwave regime. On the other hand, the desire to control the blackbody radiation has long been a research topic of interest for scientists—one particular theme being the construction of a selective emitter whose thermal radiation is much narrower than that of a blackbody at the same temperature. In this talk, I will present the computational and experimental work that was used to demonstrate infrared metamaterial absorbers and selective thermal emitters. Based on these work, we further demonstrate an electrically tunable infrared metamaterial absorber in the mid-infrared wavelength range. A voltage potential applied between the metallic portion of metamaterial array and the bottom ground plane layer permits adjustment of the distance between them thus altering the electromagnetic response from the array. Our device experimentally demonstrates absorption tunability of 46.2% at two operational wavelengths.

Parts of this thesis are based on unpublished and published articles by me in collaboration with others. The dissertation author is the primary researcher and author

in these publications. The text of chapter two, chapter five, and chapter seven is, in part, a reprint of manuscript being prepared for publication. The text of chapter three is, in part, a reprint of material as it appears in Physical review letters 104 (20), 207403. The text of chapter four is, in part, a reprint of material as it appears in Physical Review Letters 107 (4), 45901. The text of chapter six is, in part, a reprint of material as it appears in Applied Physics Letters 96, 011906

Table of Contents

Acknowledgement

First and foremost I want to thank my advisor Willie J. Padilla. Prof. Padilla is the most passionate and energetic researcher I have ever met. He is always there for me with his knowledge, patience and enthusiasm. He always encourages me when I met difficulties and be generous with praise when I made accomplishments. I thank him for giving me all the interesting projects to work with and giving me many opportunities to present my work at conferences. I am very grateful to be his student.

My sincere thanks also go to the members of my committee Prof. Michael J. Naughton, And Prof. Krzysztof Kempa for reading this dissertation and providing many valuable comments that improved the presentation and contents of this dissertation.

In regards to the Boston College nanofabrication cleanroom, I thank Steve Shepard, Dezhi Wang, and Greg McMahon for their generous help during the time I spent there for sample fabrications. Steve provides me the most extensive training on various cleanroom tools and I learn lot knowledge from him regarding semiconductor nanofabrication techniques. Dezhi trained me on how to use the SEM and e-beam lithography and these techniques significantly contributed to my projects. Greg helped me a lot for using the FIB to examine my samples.

Thanks and gratitude are also given to Chris Bingham, David Shrekenhamer, Wenchen Chen, Machhindra Koirala, Diva Murugesapillai, Kebin Fan, Weitao Dai, Salvatore Savo, Xinyu Liu, Xueyuan Wu and many others who helped me through daily research in every aspects along the way.

Last, but not least, I would like to thank my wife Mingyi Zhen for her understanding and love during the past few years. Her support and encouragement made this dissertation possible. My deepest gratitude and love is given to my parents and sisters for their dedication and unconditional support.

June 2013

Xianliang Liu

Publications

7. “Metamaterial Electromagnetic Wave Absorbers” Claire M. Watts, Xianliang Liu, Willie J Padilla Advanced Materials 23, OP98 (2012)

6. “Taming the Blackbody with Infrared Metamaterials as Selective Thermal Emitters” Xianliang Liu, Talmage Tyler, Tatiana Starr, Anthony F. Starr, Nan Marie Jokerst, and Willie J. Padilla Phys. Rev. Lett. 107, 045901 (2011)

5. “Perfect electromagnetic absorbers from microwave to optical” Willie Padilla, and Xianliang Liu Optical Design & Engineering, SPIE Newsroom, 10, 003137, (2010)

4. “High performance optical absorber based on a plasmonic metamaterial” Jiaming Hao, Jing Wang, Xianliang Liu, Willie J. Padilla, Lei Zhou, and Min Qiu Appl. Phys.Lett. 96, 251104 (2010)

3. “Infrared Spatial and Frequency Selective Metamaterial with Near-Unity Absorbance” Xianliang Liu, Tatiana Starr, Anthony F. Starr, and Willie J. Padilla Phys. Rev. Lett. 104, 207403 (2010)

2. “Metamaterials on parylene thin film substrates: Design, fabrication and characterization at THz frequencies”Xianliang Liu, S. MacNaughton, D. B. Shrekenhamer, H. Tao, R. D Averitt, M. R. Dokmeci, S.Sonkusale and W. J. Padilla Appl. Phys. Lett. 96, 011906 (2010)

1. “Planar wallpaper group metamaterials for novel terahertz applications” C. M. Bingham, H. Tao, Xianliang Liu, R. D. Averitt, X. Zhang, and W. J. Padilla Opt. Express 16(23), 1856518575 (2008)

Presentations

5. MRS Fall Meeting, Boston, MA, November 25-30, 2012.

"Controlling incandescence using Metamaterials"

4. International Workshop on Metamaterials, Nanjing, China, October 08-10, 2012.

"Tunable Metamaterial Absorber and Thermal Emitter"

3. Low Energy Electrodynamics in Solids, Napa, CA, July 22-27, 2012.

"Controlling incandescence using Metamaterials"

2. International Workshop on Electromagnetic Metamaterials IV, Albuquerque, NM, August 11-12, 2010.

"Infrared and optical metamaterial perfect absorbers"

1. SPIE Optics + Photonics, San Diego, CA, August 1-5, 2010.

"Metamaterial perfect absorbers, from microwave to infrared"

Chapter 1

Introduction

Metamaterials are fashioned from arrays of shaped conducting patterns and are able to exhibit great control over electromagnetic waves. This power stems from their ability to independently tailor both the electric and magnetic response and has led to many rapidly expanding areas of research, one of which is the metamaterial perfect absorber (MPA). MPAs are able to efficiently absorb electromagnetic radiation with negligible reflection and zero transmission. They are highly desired for frequencies above the microwave regime and may lead to novel spatial light modulators. This thesis is concerned over various topic in the metamaterial including general metamaterial absorber, spatially dependent metamaterial absorber, metamaterial selective emitter, MEMS based tunable metamaterial absorber, and other method such as studying metamaterials with group theory.

In Chapter 2, we present the design,fabrication and characterization of metamaterial absorbers (MMA) that resonant at mid-infrared (MIR) range. Experimental results show that our MMA achieves absorption as high as 99.5%. We further investigated the effect of dielectric properties of the intermediated layer to the performance of the MMA, and our simulation shows that the design of the MMA is robust that high absorption can always be achieved. Also, we explored the MMA absorption at different incident angle and simulation results shows the realizability of the high absorption MMA at large incident angles which make it plausible for application purposes.

In Chapter 3, we demonstrate, for the first time, a spatially dependent metamaterial perfect absorber operating in the infrared regime. We achieve an experimental absorption of 97% at a wavelength of 6.0 μm, and our results agree well with numerical full-wave simulations. By using two different metamaterial sublattices we experimentally demonstrate a spatial and frequency varying absorption which may have many relevant applications, including hyperspectral subsampling imaging.

In Chapter 4, we demonstrate, for the first time, selective thermal emitters based on metamaterial perfect absorbers. We experimentally realize a narrow band midinfrared (MIR) thermal emitter. Multiple metamaterial sublattices further permit construction of a dual-band MIR emitter. By performing both emissivity and absorptivity measurements, we find that emissivity and absorptivity agree very well as predicted by Kirchhoff's law of thermal radiation. Our results directly demonstrate the great flexibility of metamaterials for tailoring blackbody emission.

In Chapter 5, we experimentally realize an electrically tunable MEMS metamaterial that effectively manipulates radiation in the mid-infrared wavelength range. The metamaterial consists of an array of suspended metal-dielectric elements above a metal ground plane on a carrier substrate. A voltage applied between the metallic metamaterial array and the bottom ground plane layer permits adjustment of the distance between them thus greatly altering the electromagnetic properties. The device functions in reflection mode and experimentally demonstrates infrared reflectivity with a modulation index of 56% at a wavelength of 6.2 μm. Our device is compatible with MEMS commercial

foundries and can be incorporated with existing devices to achieve high speed infrared light modulation.

In Chapter 6, we design, fabricate, and characterize terahertz THz resonant metamaterials on parylene free-standing thin film substrates. Several different metamaterials are investigated and our results show strong electromagnetic responses at THz frequencies ranging from 500 GHz to 2.5 THz. The complex frequency dependent dielectric properties of parylene are determined from inversion of reflection and transmission data, thus indicating that parylene is an ideal low loss substrate or coating material. The biostable and biocompatible properties of parylene coupled with the multifunctional exotic properties of metamaterials indicate great potential for medical purposes such as THz imaging for skin cancer detection.

In Chapter 7, we investigate the surface current modes of metamaterials using group theory method, which is based on the symmetric properties that metamaterials possess. Using the character table of point group that the metamaterials belongs to, we demonstrate that the surface current modes of metamaterials can be predicted. Finite element program is used to simulate the the metamaterials response to electromagnetic wave and the simulation results agrees well with what we predicted by using group theory method.

In the following of this section, I will briefly discuss the computational, fabrication and characterization that were using.

Computational tools that are used to model the interaction between electromagnetic waves and materials with complex structures are very mature and thus can provide an

accurate estimation of the metamaterial performance. Many scientists in the field of metamaterials are adopting commercialized software in order to predict the behavior of their structures before engaging in fabrication. One advantage of metamaterial simulation is that an optimized structure can be designed and the behavior predicted without unnecessary fabrication iterations. Also, due to the accuracy of the simulation techniques, there is generally a good match between simulated and experimental results if the material properties are well known. Among the simulation programs, CST Microwave studio, HFSS, and Comsol are some of the most common. All the computational simulations in this dissertation utilized CST Microwave studio. Chapter 3, 4, 6 uses CST Microwave studio 2009. Chapter 2, 5, 7 uses Microwave studio 2012.

In simulations, optical properties are assigned to materials that make up the structure, such as metals and insulators. The agreement between simulation and experiment depends greatly on the accuracy of these properties in simulated materials compared to their real values. Metal is one critical part of MPAs which affects the resonating behavior. Therefore, good knowledge of metal properties in simulation is essential to obtain trustable results. At low frequencies, such as microwaves, metals such as gold and copper are modeled as good conductors with a particular value for the conductivity. However, when simulating metamaterials at higher frequencies, such as infrared or optical, metals tend to be lossier and the Drude model is often used to reproduce their frequency dependent optical properties.

In simulation, the reflectivity and transmissivity can be obtained by setting up appropriate boundary conditions and excitations. In a typical finite difference time

domain (FDTD) simulation program, either perfect electric (PE) and perfect magnetic (PM) boundary conditions with waveguide ports or periodic boundary conditions with plane waves can be used to simulate interaction between electromagnetic waves and a periodic structure. In the case of PE and PM boundary conditions, the polarization of the incident light is confined such that the electric field is polarized along the PE boundary. With the presence of two waveguide ports on either side of the structure, a TEM wave is excited and is incident on the structure. For periodic boundaries, a plane wave with a certain polarization is launched onto the structure and all fields and currents are forced to be identical at the boundaries of the simulation space. All simulation settings mentioned output the complex scattering parameters, such as the transmission coefficient, S21, and reflection coefficient, S11, from which $R(\omega)$ and $T(\omega)$ can be obtained as $T(\omega) = |S21|^2$ and $R(\omega) = |S11|^2$, respectively.

Metamaterials that operate in the microwave frequency range are normally fabricated using the printed circuit board (PCB) method in which a certain thickness of copper is deposited on both sides of a photosensitized board, FR-4 being a common example. Since, in this frequency range, the sizes of metamaterial resonators are relative large, i.e. on the order of millimeters with the smallest dimension approximately 100 μm, a photo mask can simply be printed on a transparency using a high resolution printer. After exposing to light, developing, and the post etching process, metamaterials with a pattern on one or both sides can be fabricated.

Fabricating the metamaterials at higher frequencies surpasses the capability of photolithography and thus requires a technique with a higher resolution. It has been

demonstrated that metamateirals operating in the infrared and visible range are best fabricated using techniques such as e-beam lithography and focused ion beam (FIB). These methods are capable of making structures with sizes that are on the order of tens of nanometers. However, compared to photolithography, which is a flood exposing parallel process, these methods expose the sample point by point, and are therefore are a much slower serial process. Hence, these techniques are usually used to fabricate small area samples.

For some applications at higher infrared frequencies, large area metamaterials are desirable. Although e-beam lithography and FIB have high resolution, they are both slow in terms of fabrication time. Therefore, other methods are adopted to make large area metamaterials. One method uses extreme ultraviolet (EUV) lithography at a wavelength of 193 nm. This is similar to conventional photolithography but uses the shorter wavelength of deep UV light, therefore enabling a higher resolution. Another method of fabricating large area samples is nano-imprint lithography, which utilizes a reusable mold.

Different techniques are used to characterize the performance of MPAs at different frequencies. In the microwave range, characterization is usually carried out in a microwave anechoic chamber where horn antennas, connected to a vector network analyzer, detect reflected and transmitted microwaves from a sample. To measure the reflectivity from a metamaterial, one microwave horn focuses the microwave beam on the sample, and another horn serves as the detector; the two horns are placed symmetrically on either side of the plane normal to the sample surface. For transmissivity measurements, the source horn is placed in front of the sample and the detector horn is

placed on the opposite side of the sample. Normalized reflectivity measurements are obtained by using a piece of metal the same size as the sample as a reference. For characterization of normalized transmissivity, an aperture is placed in front of the sample, and measurements are divided by the transmissivity of the same open aperture.

Terahertz time domain spectroscopy (TDS) is another powerful tool to characterize the performance of MPAs, especially at THz frequencies. By Fourier transforming the time pulse from the sample and reference, both amplitude and phase information can be obtained. Fourier transform infrared (FTIR) spectroscopy is the most frequently used method to characterize MPAs working in ranges higher than microwave and covers an extremely broad spectrum ranging from THz to visible. Different combinations of sources, beam splitters, and detectors are used to operate the system most efficiently within a certain frequency range.

Although conventional FTIR spectroscopy is extremely broad band, it requires relatively large sample areas due to available, diffraction limited, spot sizes. However, at high frequencies such as infrared and visible, samples are generally fabricated using e-beam lithography. It is therefore highly preferable to make relatively small sample sizes, owing to the long fabrication times discussed above. None-the-less, an infrared microscope that is coupled to a FTIR system can accurately characterize such small samples. In the coupled system, the FTIR spectrometer is used as the light source (interferometer) and the beam is guided into the microscope where it can be focused to a high quality near diffraction limited spot. Typical designs use an adjustable aperture at a conjugate image in order to control the size of the light spot illuminating the

sample.Many IR microscopes are catoptric systems, and thus able to characterize materials over the same large bandwidth as the source–THz to optical in the case described above.

Chapter 2

Metamaterial Absorbers for the Infrared

2.1 Introduction

Metamaterials have attracted increasing attention in the past decade due to their unique ability to engineer exotic electromagnetic responses. One intriguing property, negative refractive index, was first theoretically predicted by Veselago in 1968 [1] and experimentally demonstrated in 2000 [2]. Although much early research in metamaterials was largely motivated by the quest for demonstration of an optical negative index of refraction [3-8], other exotic effects drove parallel developments - examples such as invisibility cloaks [9] and perfect lenses [10, 11]. Recently a new development - the so called `metamaterial absorber' - was demonstrated to achieve near-unity absorption in nearly any range of the electromagnetic spectrum and may be added to the list of unique electromagnetic responses achievable with metamaterials.

The advent of the metamaterial absorber (MMA) has spawned a new direction of research within the general metamaterials community. Interest stems from the ability of the metamaterial absorber (MMA) to yield tailored frequency dependent absorption. A simple design leads to a robust, highly efficient, versatile and agile absorber. The absorptive response can easily be specified – either in amplitude or frequency - by changing the shape and size of the metamaterial structure which allows for tuning both the electric [$\varepsilon(\omega)$] and magnetic [$\mu(\omega)$] response.

The first MMA was computationally and experimentally realized at microwave frequencies by means of sandwiching a thin layer of dielectric between an electric ring resonator [12, 13] and a cut wire [14]. Soon afterwards, follow-on work extended operation of the MMA to THz frequencies [15], infrared [20] and optical [22, 23] ranges. Studies were also carried out to explore the polarization dependence [16] and incident angle dependence [17, 18] of the MMA. Other works include fabrication of free standing MMA films, which give flexible designs ideal for potential applications [19], and more recently MMAs' use as selective thermal emitters [21] have been experimentally demonstrated which have great potential for energy harvesting applications.

In this work, we present a comprehensive study of MMAs operating at MIR frequencies. We simulated, fabricated and characterized a set of samples whose resonances span from 6-11 μm. Dependence of the electromagnetic absorption on metal property, dielectric material property and incident angle is investigated. Details of the microscopic loss mechanism within the constituent materials are also revealed. Several factors that affect the MMA performance were studied. Our simulations and experimental results show good agreement and we were able to achieve absorptions as high as 99.5%.

2.2 Design

2.2.1 Design theory

Electromagnetic wave incident on a material may be reflected R, transmitted T, absorbed A or scattered. The specific frequency dependent relationship between these quantities is, if ignoring scattering, $A(\omega) = 1 - T(\omega) - R(\omega)$. Thus in order to realize a

particular value for the absorption A0 at a desired operational frequency ω_0, one needs to specify the exact values for R and T at ω_0. A MMA with unity absorption would thus require zero reflection and zero transmission. At normal incidence, the reflection from a surface is determined by $R(\omega) = |(Z(\omega) - Z(0)) / (Z(\omega) - Z(0)|^2$, where $Z(\omega) = Z_1(\omega) + iZ_2(\omega)$ is the complex impedance of the material, and Z_0 is the impedance of free space. A surface which is impedance matched at a particular frequency to free space ($Z(\omega_0) = Z_0$) will thus yield zero reflection.

The transmission coefficient $t(\omega)$ for a normally incident electromagnetic wave at an interface in terms of the impedance $Z(\omega)$ and effective refractive index $n(\omega)=n_1(\omega)+in_2(\omega)$ is described as [24],

$$\tilde{t}(\omega) = [\cos(nkd) - \frac{i}{2}\left(\frac{Z}{Z_0} + \frac{Z_0}{Z}\right)\sin(nkd)]^{-1} e^{-ikd}$$

where $k=\omega/c$ is the wavenumber of incident waves and d is the slab thickness. If we have the case of perfectly matched impedance, i.e. ($Z(\omega_0) = Z_0$), then Eq. (1) reduces to,

$$\tilde{t}(\omega) = [\cos(nkd) - i\sin(nkd)]^{-1} e^{-ikd}$$

and we find the transmission coefficient reduce to,

$$\tilde{t}(\omega) = e^{-i(n_1-1)kd} e^{-n_2 kd}$$

therefore the transmission is described by,

$$T(\omega) = |\tilde{t}(\omega)|^2 = e^{-2n_2 kd}$$

where n2 is the imaginary portion, determining the lossy properties, of the effective refractive index for the MMA. In order to achieve unity absorption, we are left with realizing impedance matching condition $Z(\omega_0) = Z_0$ and making n_2 large. Since the

impedance and refractive index of a material is related to the electric permittivity ε (ω) and magnetic permeability μ (ω) as $Z(\omega) = \sqrt{\mu(\omega)}/\varepsilon(\omega)$ and $n(\omega) = \sqrt{\mu(\omega)}\,\varepsilon(\omega)$, the ability of metamaterials to independently tailor ε (ω) and μ (ω) make it possible to simultaneously tune $Z(\omega)$ and $n_2(\omega)$, thus making the realization of 'perfect absorption' possible.

In our particular MMA design, shown schematically in Fig. 1(a) and (b), we utilize a three layer structure which consists of two metal elements and an intermediate dielectric spacer. The top cross resonator is a type of electric ring resonator (ERR) [25] and couples only to the electric component of the electromagnetic field which permits tuning of the frequency dependent permittivity ε (ω). The metal-dielectric-metal configuration responds to time varying magnetic fields - a result of antiparallel currents oscillating between the cross resonator and the ground plane, and is well characterized by a frequency dependent magnetic response μ (ω). By manipulating both ε and μ, it is possible to tune the impedance $Z(\omega) = \sqrt{\mu(\omega)}/\varepsilon(\omega)$ of the MMA to match the impedance Z_0 (ω) of free space, thus minimizing the reflectance. Meanwhile, the imaginary portion of refractive index n_2 is tuned simultaneously to be very large to absorb all the energy that incident on the MMA. The existing of the continues ground plane doubles the effective slab thickness d in equation 4 and further increase the absorption effciency. Also since the ground plane is opaque for infrared light, it prevent light from going through, thus provides zero transmission. These conditions thus lead to high absorption.

The resonant electromagnetic response of metamaterials scales with dimension of the structure. This implies that, to first order, the same metamaterial design can be used in all frequency bands by simply adjusting the size. Thus in principle, it should be trivial to realize MMAs at higher frequencies for example, at infrared and optical, by simply miniaturizing a given microwave or terahertz design. However, the electromagnetic properties of the constituent materials may be drastically different at higher frequencies. For example dielectric materials often have optically active phonons which occur in the far infrared range (100-1000 cm^{-1}, 3-30THz), whereas polymers usually have vibrational

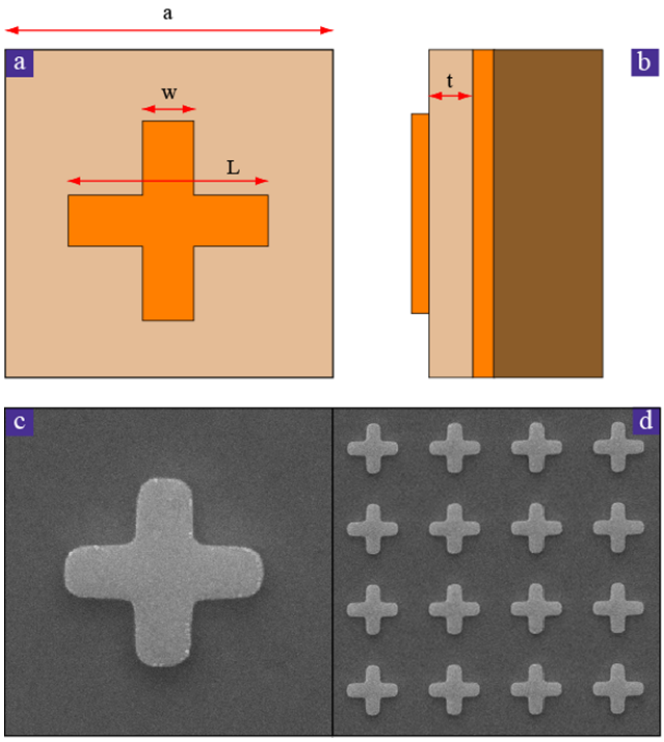

FIG. 1. Design and fabrication of the infrared MMA. (a), Schematic of a MMA unit cell and its optimized dimensions are a = 3.2, l = 1.9, w = 0.5, t = 0.2 in micrometer. (b), Side

view of the unit cell. (c), Scanning Electron Microscope (SEM) image of one unit cell. (d), SEM image of a periodically patterned array.

or rotational modes which occur within the MIR range. Although most metals may be considered good conductors, i.e. lossless, at microwave frequencies, they become transparent at the plasma frequency, which typically occurs at optical or UV wavelengths. Perhaps a greater limiting factor, however, is the great reduction in conductivity values for metals which occurs at their scattering frequency - about 10 THz for most metals. These factors need to be considered when designing a MMA for high frequency operation.

2.2.2 Specular simulation

To study the performance of a MMA for operation in the MIR, we perform full wave three dimensional electromagnetic simulations using a commercial finite difference time domain (FDTD) program. A TEM wave incident upon a single unit cell of the metamaterial is approximated by utilizing perfect electric and perfect magnetic boundary conditions. Two wave ports are setup on both sides of the structure to generate a plane wave at normal incidence. All metallic portions (cross resonator and ground plane) of the metamaterial are modeled as gold using a frequency dependent Drude model with a plasma frequency $\omega_p = 2\pi \times 2.175 \times 10^3$ THz and collision frequency $\omega_c = 2\pi \times 6.5$ THz [26]. The insulating layer (lying in-between the two metal structures) is modeled as a frequency independent lossy dielectric, with a real part of $\varepsilon_1 = 1.95$ and a loss tangent of

tan δ = 0.02. The time domain solver is used to determine the reflection S11 (ω) and transmission S21 (ω) coeffcients of the metamaterial unit cell. Absorption is calculated as $A(\omega) = 1 - |S_{11}(\omega)|^2 - |S_{21}(\omega)|^2$. As expected simulations indicate that the transmittance $T = |S_{21}(\omega)|^2$ is effectively zero across the entire frequency range due to the ground plane. The reflectance $R = |S_{11}(\omega)|^2$ is relatively high except where the metamaterial obtains an impedance match to free space, and a minimum occurs.

We discuss one particular MMA design in order to give specific dimensions for MIR operation. The MMA shown in Fig. 1 achieves a simulated absorption of 99.9% at 5.9 μm, and have dimensions of, (in microns): a = 3.2, l = 1.9, w = 0.5, t = 0.2. The thickness of the top metal layer and ground plane are 0.075 μm and 0.1 μm, respectively. The

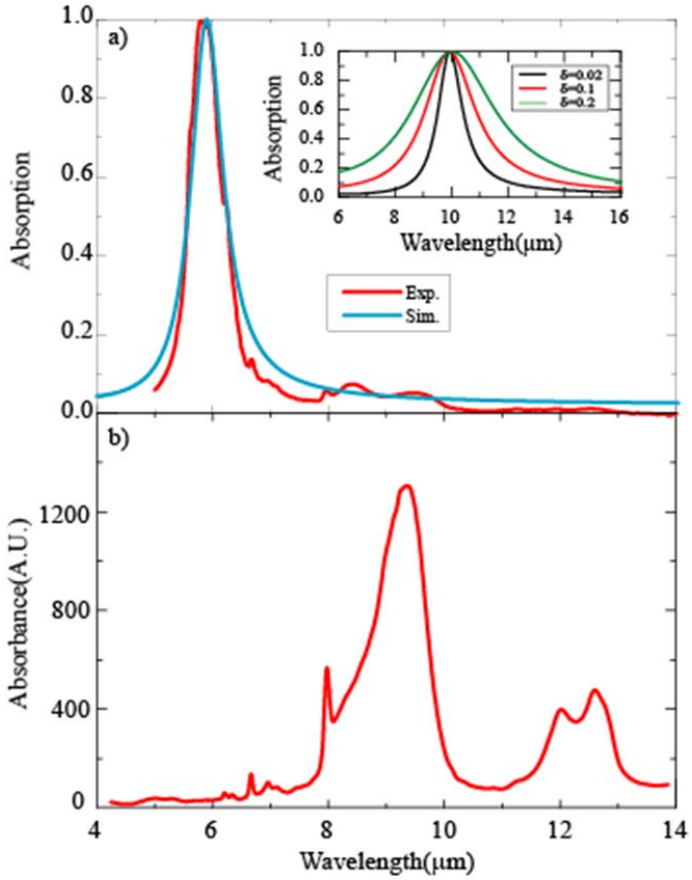

FIG. 2. (a) A comparison between the experimental absorption (red) and simulated absorption (blue). The maximum absorption at 5.91 μm is 99.5%. Inset shows two different simulations of MMA designed to have a maximum absorption at 10 μm with dielectric loss tangent of δ=0.1 for the red curve and δ=0.2 for the green curve. (b) Absorption coefficient of BCB.

simulated A (ω) with this dimension is shown as the blue curve in Fig. 2. Based on this MMA design, we modify the dimension of the unit cell and cross resonator to study its

effect on the resonant wavelength. In simulation this is accomplished by performing parameter sweeps of a and l.

Although simulated values for the absorption are near 100% at normal incidence, A (ω) must drop as we move to grazing incidence angles - owing to the Fresnel equations. The particular functional form of the angular dependence of the absorption was investigated computationally. Periodic boundary conditions with floquet ports are used in which case the incident angle can be specified between 0 and 90º. The angular dependent absorption of MMA for Both TE and TM light are studies at various incident angles.

2.2.3 Dielectric loss tangent dependence

In order to clarify the dependence of the absorption on the dielectric loss, we performed a computational study as function of dielectric material loss tangent. In simulation, we manually modify the dielectric material property by modifying the loss tangent of the dielectric spacing layer material. It is found that the maximum value of the absorption, resonance frequency and bandwidth of the absorption all change correspondingly. We chose to change the length of the resonator (L) and thickness (t) of the dielectric spacer in order to return both the resonant frequency and maximum absorption to their original values, i.e. as close as possible to those before modifications. When increasing the loss tangent, the location of the peak absorption shifts to longer wavelength and the value of the absorption peak becomes lower, therefore we decrease the resonator length and increase the thickness of the dielectric spacer to compensate the changes in the absorption. Although this is possible in each case, the bandwidth of the

resonance has the general property that it increases for increasing loss tangent. The inset to Fig. 2 shows three different simulations of metamaterials designed to have a maximum

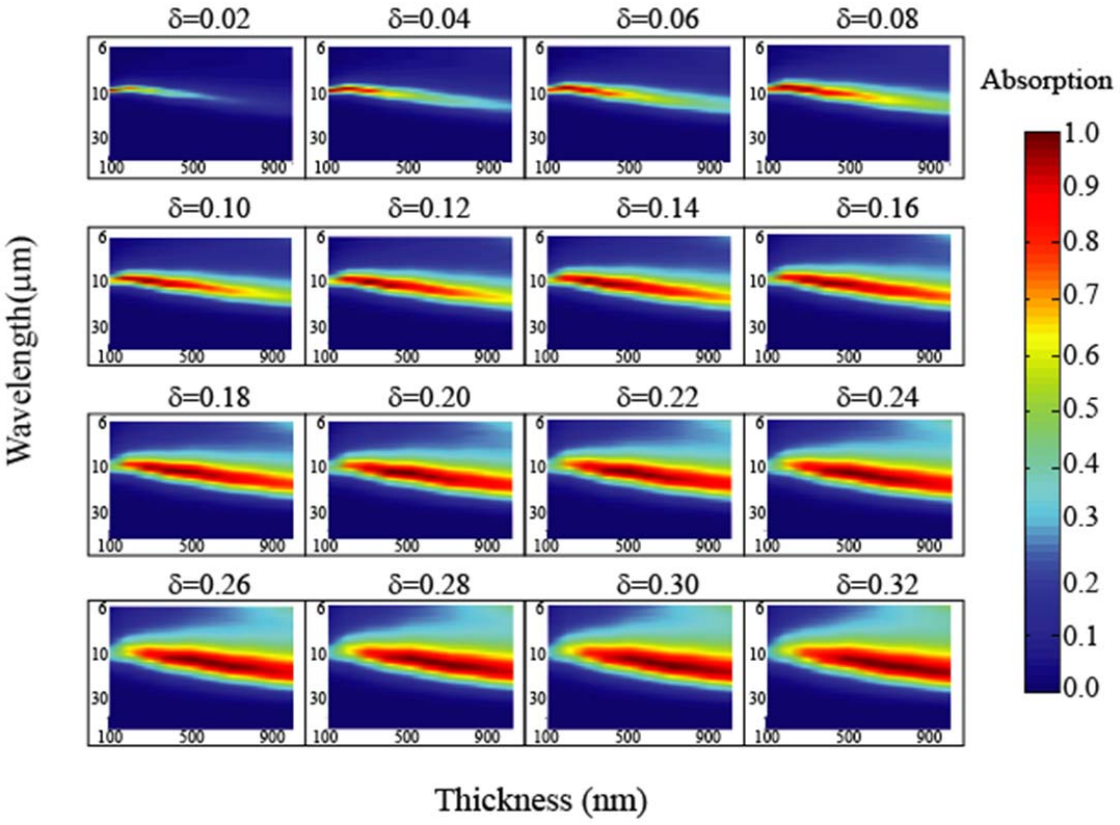

FIG. 3. A systematic study of MMA performance dependence on di®erent loss tangent value and dielectric spacer thickness. X axis is the thickness of dielectric layer and y axis is wavelength. Absorption is indicated by the color scale.

absorption at 10 μm wavelength. The loss tangent is δ=0.02 for the black curve and δ=0.1, 0.2 for the red and green curves, respectively. Results clearly show the absorption peak gets broadened when loss tangent increases.

Since modifying the loss tangent of the dielectric spacer changes both the resonance frequency and absorption strength which require tuning other dimension parameters to re-optimize the MMA, we performed a full simulation investigation. In this study, we study the relation between dielectric loss tangent δ, spacer thickness, resonance frequency and absorption strength. We again study a metamaterial absorber optimized to obtain peak absorption near 10 μm. As shown in Fig. 3, sixteen sets of simulations were performed with variation of the loss tangent from 0.02 to 0.32 with a step of 0.02. In each set ten simulations are carried out with different dielectric layer thicknesses ranging from 100nm to 1μm. Each sub-panel plots the absorption, (as indicated by the color), and the vertical axis is the wavelength, the horizontal axis is the thickness of the dielectric spacer, and each sub-panel is for different assumed values of the loss tangent, as indicated.

TABLE I. Loss distribution for combination of different metals and dielectric materials.

	Dielectric properties	Dielectric loss P_d	Ohmic loss P_o	P_d/P_o
PEC	1.95+0i	0	0	N/A
	1.95+0.02i	0.476	0	N/A
	1.95+0.1i	0.537	0	N/A
Drude Au	1.95+0i	0	0.279	0
	1.95+0.02i	0.210	0.177	1.19
	1.95+0.1i	0.427	0.07	6.1
Drude Al	1.95+0i	0	0.355	0
	1.95+0.02i	0.176	0.250	0.70
	1.95+0.1i	0.368	0.09	4.09

2.3.4 Loss distribution in metal and dielectric

Previous work has shown that majority of the energy absorbed in the MMA is dissipated as heat in the dielectric layer for a particular combination of metal and dielectric properties at MIR frequencies [20]. Dielectric losses were found to be an order of magnitude larger than Ohmic losses within the metallic portions of the MMA at THz. Thus properties of the dielectric layer play an important role in determining the performance of MMAs. Although at long wavelengths metals may be regarded as perfect electric conductors', at shorter wavelengths this is not necessarily true. Therefore to obtain a comprehensive understanding of how loss is distributed in the different components that constitute a MMA, it is necessary to monitor energy dissipated within the constituent materials.

From operational wavelength point of view, metals are good conductors at long wavelength and become lossy at shorter wavelength. This fact determines how the absorbed energy within the MMA distributes between Ohmic loss and dielectric loss. Generally speaking, at long wavelength such as Microwave range, Ohmic loss dominate in the absorption process while at short wavelength such as near infrared, majority of the loss goes to dielectric portion as dielectric loss. In the wavelength of interest for our investigation, mid infrared range, a meaningful study is to investigate the loss distribution when using different metallic and dielectric materials. To study the rolls that metals and dielectric material play in the absorption mechanism of the MMAs, we decide to use different metals and dielectric materials for the metallic portion and the dielectric spacer correspondingly. In this computational study, we chose three different metals which are

PEC, gold, and silver. For the dielectric material, we only manipulate the loss property in which case we change the loss tangent value in simulation. The simulated results for MMAs made up of different metal and dielectric materials are shown in Fig. 4. The metallic materials in Fig. 4(a,) (b), and (c) are PEC, Drude gold and Drude aluminum, respectively. The plasma frequency of Drude gold is $\omega_p=2\pi \times 2.175 \times 10^3$ THz and collision frequency is $\omega_p=2\pi \times 6.5$ THz while the plasma frequency of Drude aluminum is

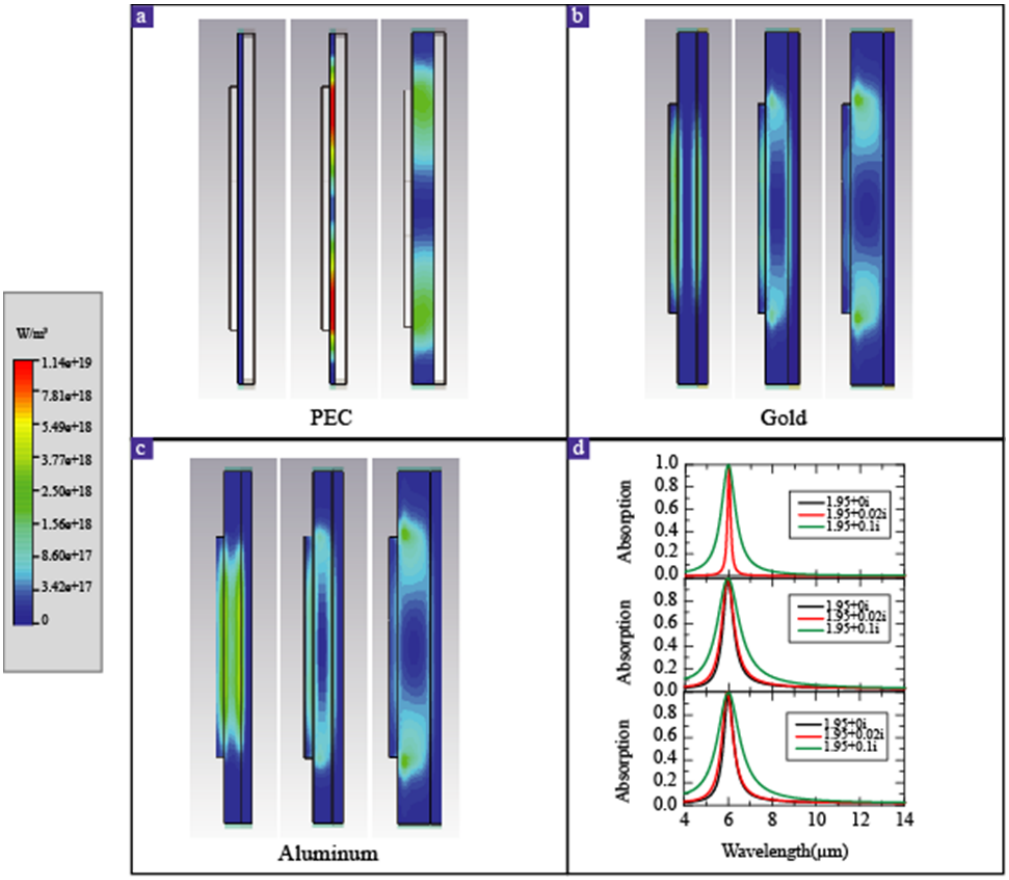

FIG. 4. Loss dissipation of MMA with different metal and dielectric materials. (a) The MMA is composed of PEC and dielectric material with loss tangent of 0, 0.02 and 0.1 for first , second and third panel correspondingly. (b) The MMA is composed of Drude gold

and dielectric material with loss tangent of 0, 0.02 and 0.1. (b) The MMA is composed of Drude aluminum and dielectric material with loss tangent of 0, 0.02 and 0.1.

$\omega_p=2\pi \times 3.6 \times 10^3$ THz and collision frequency is $\omega_p=2\pi \times 19.2$ THz [26]. For each metal, a dielectric material with the same $\varepsilon_1=1.95$, but different loss tangents are used. The loss tangents for the dielectric material are 0, 0.02 and 0.1 correspondingly. Nine simulations are performed and in each case, the absorption is maximized (except first panel of Fig. 4 (a)) at 6 μm and we use loss distribution monitor to detect how loss is dissipated in each layer.

TABLE II. Dimensions of the nine MMA samples and the resonant wavelength and the maximum absortivity for each sample.

	a (μm)	l (μm)	w (μm)	t (μm)	λ_0 (μm)	A_{max}
Sample 1	4	3.55	0.5	0.2	10.96	76%
Sample 2	4	3.35	0.5	0.2	10.48	80%
Sample 3	4	3.15	0.5	0.2	10.13	73%
Sample 4	4	2.95	0.5	0.2	8.8	77%
Sample 5	3.2	2.75	0.5	0.2	8.36	95%
Sample 6	3.2	2.55	0.5	0.2	7.65	99%
Sample 7	3.2	2.35	0.5	0.2	7.14	99%
Sample 8	3.2	2.15	0.5	0.2	6.51	96%
Sample 9	3.2	1.95	0.5	0.2	5.91	97%

Fig. 4(a,) (b), and (c) displays the cross section of the loss distribution in each layer of the MMA structure whose metal layers are PEC, gold and aluminum correspondingly. The loss distribution in each case is indicated by the color map. In each plot, there are three subplots that correspond to different loss tangents of the dielectric layer; the values

being 0, 0.02, and 0.1 from left to right. We observe that thicker dielectric spacer is needed to achieve the same high absorption when increasing the loss tangent, which is consistent with results shown in Fig. 3. We notice that high absorption can always be achieved with either one of the metal or dielectric or both being lossy. However, when metal and dielectric are both lossless, there will be no absorption in the structure as indicated by the first subplot in Fig. 4(a) and black curve in first subplot of Fig. 4(d). The quantitative results are shown in Tab. I which contains the loss power in each layer of the MMA structure with different metal and dielectric materials.

2.3 Fabrication and characterization

2.3.1 Fabrication

The MMA samples are fabricated by a layer-on-layer process using deep UV lithography. As shown in the schematic in Fig. 1, the bottom layer is 100 nm thick gold and is deposited using electron beam evaporation on top of a silicon substrate. Next a layer of benzocyclobutene (BCB) is spin coated and UV cured to a thickness of 180 nm. Then photo resist is spin coated on top of BCB and patterned using the 193nm deep UV step and scan system. The top gold metamaterial structure is deposited using electron beam evaporation followed by a lift off process. Nine samples with distinct resonator

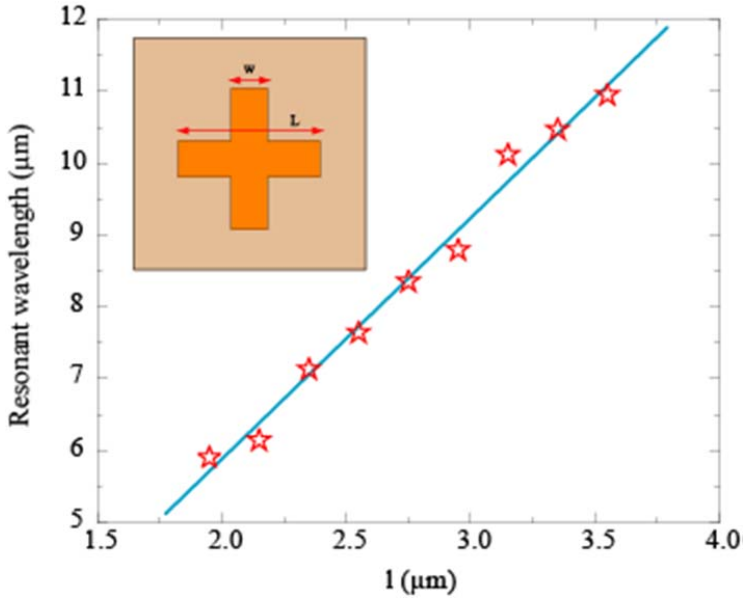

FIG. 5. MMA resonance frequency as a function of the cross resonator length. The red stars shows the experimental results and the blue one is a fitted line.

lengthes are fabricated on the sample wafer whose dimensions are listed in Tab. II The SEM images of one fabricated sample is displayed in Fig. 1(c) and (d).

2.3.2 Characterization

The transmission and reflection of the fabricated MMAs are characterized using a Fourier-transform infrared spectrometer combined with an infrared microscope. A liquid nitrogen cooled mercury cadmium telluride (MCT) detector, a 15X cassegrain objective, and a potassium bromide (KBr) beam splitter was utilized in the experimental setup. The reflection is measured at an incident angle of 21.8 degrees and transmission is measured at normal incidence. An adjustable knife edge aperture is used to ensure that the reflected

signal is due only to the sample under investigation. The measured reflection spectra are normalized with respect to a gold mirror while the transmission spectrum is normalized with respect to an open aperture of the same area. The measured transmission and reflection are then used to calculate the absorption. The experimental absorption of one MMA is shown in Fig. 2 as the red curve. If we take, as our point of evaluation, the full width at half max, we find that the absorber has a span of about 0.75 μm compared to the center wavelength of 5.88μm - i.e. a bandwidth of about 12%. As is evident from Fig. 2, we achieve good agreement between experimental (red) and simulated (blue) absorptions. As seen from the experimental data of Fig. 2(a), there are some little features at longer wavelength, which is due to the intrinsic absorption of the dielectric material of BCB. Fig. 2(b) shows the absorbance of the BCB in the same wavelength range and it clearly show that there are some absorption peaks in this wavelength range and this well explains the features in the experimental absorption of Fig. 2(a).

Besides the sample discussed above, eight other infrared MMAs were fabricated and investigated as well, all using the same experimental procedure described previously. The lengths (L) of the MMA cross resonators were varied from 1.75 μm to 3.75 μm. The dimensions of the nine samples are listed in Tab. II. A plot of the resonance frequency as a function of the cross resonator length is displayed in Fig. 5 indicating that these samples yield absorption resonances that cover a wide range within the infrared regime, from 6 μm-11 μm. The red stars show the experimental results and the blue line is a fitted line. As can be observed the resonance wavelength varies linearly with increasing the side length of the MMA.

2.3.3 Angular dependent absorption

Angular dependent absorption property is an important characteristic of MMA which has been investigated in THz [17, 18]. So far, all the MMA studied in this work is

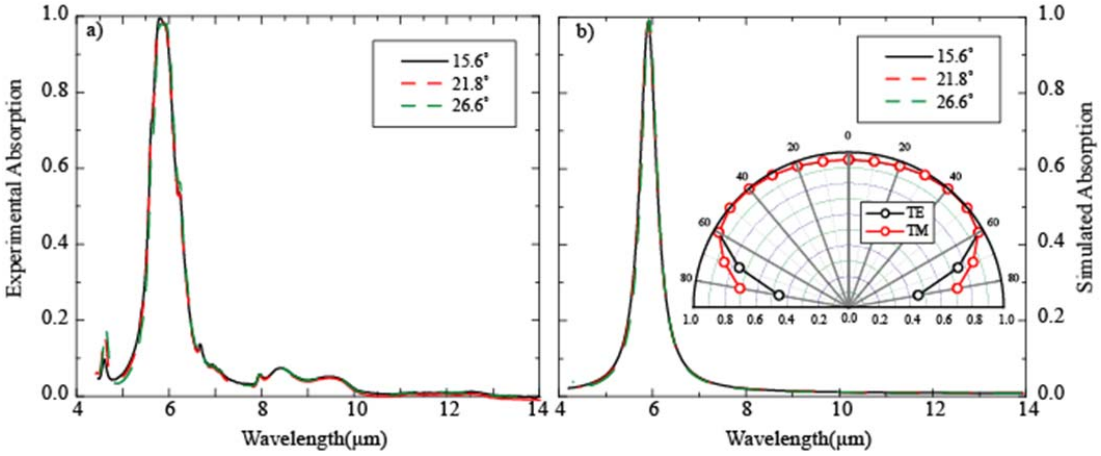

FIG. 6. (a), Experimental measured absorption as function of wavelength at different angle of incidence. (b), Simulated absorption at different angle of incidence. Inset shows the simulated absorption peak value as function of incident angle for both TE and TM wave for the same structure.

optimized at normal incident which means the MMA offers highest absorption when the incident light is perpendicular to the MMA surface. In certain applications, maintaining high absorption to a large incident angle is desirable to absorb light come from a large solid angle. To investigate the angular dependent absorption of our MMA design, we performed both computational and experimental studies.

In experiment, the same experimental setup is used to investigate the angular dependence of the MMA by measuring the reflection at various incident angles. A

number of distinct microscope reflective objectives with different numerical apertures are used to study the absorption at distinct incident angle. Three off-angle reflection measurements were performed with 15.6 º, 21.8 º and 26.6 º incident angle objectives. We as well simulated the off - angle absorption at these three angle. The experimental and simulated results are displayed in Fig. 6(a) and (b), respectively. Due to the limitation of sample size and experimental setup, we can only characterize the absorption of these three angles of incidence. However, in simulation we studied off-angle absorption for various angles ranging from normal incidence up to 80 º. The inset to Fig. 6(b) shows the simulated peak absorption value as a function of incident angle for both TE and TM polarized light. The results clearly demonstrate that the high absorption achieved by the MMA at normal incidence is well preserved to large off angles. At an incident angle of 70 degrees the MMA has absorption of 75% for TE waves and 85% for TM waves.

2.4 Discussion and conclusion

Our study shows that the thickness and dielectric properties of the intermediate spacer layer is crucial for the MMA absorption performance. For example Fig. 3 demonstrates that although the loss tangent for the dielectric layer is varied by over an order of magnitude from 0.02 to 0.32, we are still able to tune the thickness of the spacing layer to achieve high absorption. This combined with the ability to tune the side length of the cross resonator gives great flexibility in the design of MIR MMAs. We can draw several conclusions from the plot shown in Fig. 3: first of all, the plot shows the MMA design is

very robust that high absorption can always be achieved with practical loss tangent. Also, absorption is less sensitive to the thickness of BCB layer when loss tangent is large. Besides, the resonance becomes broadened when loss tangent change from low to high, which means the lower the loss, the sharper the resonance is. These simulations shows great flexibility of the MMA that materials with different loss tangent can be used for MMA design to achieve high absorption.

We show that loss distribution loss distribution as ohmic loss and dielectric loss are highly dependent on the material that being used for MMA as shown in Tab. I. For example, using a very lossy dielectric material with large loss tangent will yield large percentage dielectric loss than ohmic loss. On the contrary, a MMA with high absorption can still be realized even when there is no loss in the dielectric, in which case all the loss are dissipated as ohmic loss. This provides us a guide line to predict how the loss dissipated in different materials in a MMA design. Generally speaking, to achieve a perfect absorbing condition, we only need either metal or dielectric being lossy. For example in Fig. 4(a), metal is PEC with no loss and in Fig. 4(b)(c) ¯rst panel, dielectric is lossless, the perfect absorbing can still be achieved. With both metal and dielectric lossless as first panel of Fig. 4(a) shows, absorption is 0 across the whole wavelength range.

In conclusion, we present the design, fabrication, and characterization of MIR metamaterial absorbers that, experimentally, obtains absorption of up to 99.5 % at 5.9 μm. we investigated how the loss properties of the intermediated layer and metals affects the performance of the MMA, and our simulation shows that the design of the MMA is

robust that high absorption can always be achieved as long as using practical loss tangent. Further, we explored the MMA behavior at different incident angle and results shows the high absorption preserves at large incident angle which make it plausible for application purpose.

Bibliography

[1] V. G. Veselago, Sov. Phys. Usp. 10, 509 (1968).

[2] D. R. Smith, W. J. Padilla, D. C. Vier, S. C. Nemat-Nasser, and S. Schultz, Phys. Rev. Lett. 84, 4184 (2000).

[3] V. M. Shalaev, W. S. Cai, U. K. Chettiar, H.-K. Yuan, A. K. Sarychev, V. P. Drachev, and A. V. Kildishev, Opt. Lett. 30, 3356 (2005).

[4] S. Linden, C. Enkrich, M.Wegener, J. F. Zhou, T. Koschny, C. M. Soukoulis, Science 306, 1351 (2004).

[5] S. Zhang, W. Fan, N. C. Panoiu, K. J. Malloy, R. M. Osgood, and S. R. J. Brueck, Phys. Rev. Lett. 94, 137402 (2005).

[6] T. J. Yen, W. J. Padilla, N. Fang, D. C. Vier, D. R. Smith, J. B. Pendry, D. N. Basov and X. Zhang, Science 303, 1494 (2004).

[7] M. Bayindir, K. Aydin, E. Ozbay, P. Marko, and C. M. Soukoulis, Appl. Phys. Lett. 81, 120 (2002).

[8] M. C. K. Wiltshire, J. B. Pendry, I. R. Young, D. J. Larkman, D. J. Gilderdale, and J. V. Hajnal, Science 291, 849 (2001).

[9] D. Schurig, J. J. Mock, B. J. Justice, S. A. Cummer, J. B. Pendry, A. F. Starr, and D. R. Smith, Science 314, 977 (2006).

[10] J. B. Pendry, Phys. Rev. Lett. 86, 3996 (2000).

[11] N. Fang, H. Lee, C. Sun, and X. Zhang, Science 308, 534 (2005).

[12] W. J. Padilla, A. J. Taylor, C. Highstrete, M. Lee, and R. D. Averitt, Phys. Rev. Lett. 96, 107401 (2006).

[13] D. Schurig, J. J. Mock, and D. R. Smith, Appl. Phys. Lett. 88, 041109 (2006).

[14] N. I. Landy, S. Sajuyigbe, J. J. Mock, D. R. Smith, and W. J. Padilla, Phys. Rev. Lett. 100, 207402 (2008).

[15] H. Tao, N. I. Landy, C. M. Bingham, X. Zhang, R. D. Averitt, and W. J. Padilla, Opt. Express 16, 7181 (2008).

[16] N. I. Landy , C. M. Bingham, T. Tyler, N. Jokerst, D. R. Smith, and W. J. Padilla, Phys. Rev. B 79, 125104 (2009).

[17] H. Tao, C. M. Bingham, A. C. Strikwerda, D. Pilon, D. Shrekenhamer, N. I. Landy, K. Fan, X. Zhang, W. J. Padilla, and R. D. Averitt, Phys. Rev. B 78, 241103(R) (2008).

[18] Y. Avitzour, Y. A. Urzhumov, and G. Shvets, Phys. Rev. B 79, 045131 (2009).

[19] H. Tao, A. C. Strikwerda, K. Fan, C. M. Bingham, W. J. Padilla, X. Zhang and R. D. Averitt, J. Phys. D: Appl. Phys. 41, 232004 (2008).

[20] X. L. Liu, T. Starr, A. F. Starr, and W. J. Padilla, Phys. Rev. Lett. 104, 207403 (2010).

[21] X. L. Liu, T. Tyler, T. Starr, A. F. Starr, N. M. Jokerst, and W. J. Padilla, Phys. Rev. Lett. 107, 045901 (2011).

[22] J. M. Hao, J. Wang, X. L. Liu, W. J. Padilla, L. Zhou, and M. Qiu, Appl. Phys. Lett. 96, 251104 (2010).

[23] N. Liu, M. Mesch, T. Weiss, M. Hentschel and H. Giessen, Nano Lett. 10, 2342 (2010).

[24] D. R. Smith, S. Schultz, P. Markos and C. M. Soukoulis, Phys. Rev. B. 65, 195104 (2002).

[25] W. J. Padilla, M. T. Aronsson, C. Highstrete, A. J. Taylor and R. D. Averitt, Phys. Rev. B. 75, 041102(R) (2007).

[26] M. A. Ordal, L. L. Long, R. J. Bell, S. E. Bell, R. R. Bell, R. W. Alexander, Jr., and C. A. Ward, Appl. Opt. 22, 1099 (1983).

Chapter 3

Infrared spatial and frequency selective metamaterial with near-unity absorbance

We demonstrate, for the first time, a spatially dependent metamaterial perfect absorber operating in the infrared regime. We achieve an experimental absorption of 97% at a wavelength of 6.0 μm, and our results agree well with numerical full-wave simulations. By using two different metamaterial sublattices we experimentally demonstrate a spatial and frequency varying absorption which may have many relevant applications, including hyperspectral subsampling imaging.

Since the first experimental demonstration of negative refractive index [1–4], research into metamaterials has grown enormously. The ability of metamaterial to achieve nearly any electromagnetic response in nearly any frequency band suggests many exotic applications including invisibility cloaks [5] and perfect lenses [6, 7]. One current expanding field of research is that of metamaterial perfect absorbers (MPAs) due to their unique ability to achieve unity absorption with high efficiency [8]. Here we present a computational and experimental study of an infrared metamaterial absorber which realizes 97% absorption at 6.0 μm wavelength. By using two different metamaterial sublattices consisting of a MPA and a near zero absorber, we experimentally demonstrate a spatial and frequency varying absorption which may have many relevant applications.

Metamaterials, through changes of the size and shape of subwavelength metallic elements, permit the amplitude and frequency tuning of both the electric [ε (ω)] and magnetic [μ (ω)] response of electromagnetic radiation. Although this electromagnetic response is resonant and narrow band, there have been demonstrations of exotic metamaterials operating in all relevant bands for frequencies below visible [9–14].

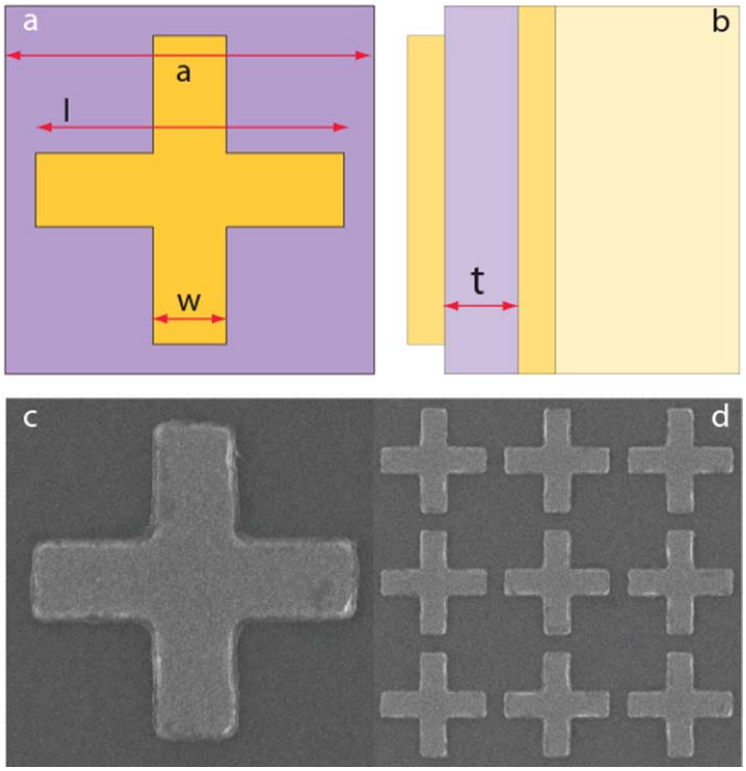

FIG. 1. Design and fabrication of the infrared metamaterial absorber. (a) Schematic of a MPA unit cell and its optimized dimensions are a = 2, l = 1.7, w = 0.4, t = 0.185 in micrometers. (b) Side view of the unit cell. (c) Scanning electron microscope (SEM) image of one unit cell. (d) SEM image of a periodically patterned array.

The resonant nature of metamaterials results in a strong focusing of the electric field within gaps of the structure, thus providing a means to dynamically control the resonance frequency, phase, and amplitude [15–17]. By using either passive or active external stimuli, temperature, electric field, optical, etc., dynamical MPAs may be explored and extended to much of the electromagnetic spectrum [18, 19]. After first demonstration of the microwave MPA, many efforts have focused on extending highly absorbing metamaterials to smaller wavelengths. To date, most studies have been carried out in the terahertz regime and absorptions as high as 96.8% have been achieved [18].

Currently, there is great interest in single-pixel imaging, based on the theory of compressive sensing [20–22]. Typically, experimental realization of these systems utilizes spatial light modulators (SLMs) for encoding random spatial patterns in the wave front of transmitted or reflected optical radiation [23, 24]. In the THz frequency regime metamaterials have shown promise to be used as SLMs in a transmission configuration [25]. At visible wavelengths single-pixel imagers may use liquid crystals or microelectromechanical systems to manipulate the spatial profile of the beam. However, at lower infrared frequencies liquid crystals are inefficient, thus preventing their use. Further, for many applications, mechanical manipulation of the incoming image may not be feasible. An intriguing application of metamaterial absorbers would be their use as a SLM in a subsampling infrared imaging system. However, to date, metamaterial absorbers have only been demonstrated in the microwave and THz frequency regimes.

The schematic of a single unit cell of an infrared MPA is shown in Figs. 1(a) and 1(b), and consists of two metallic elements: a cross-shaped resonator and ground plane. We

space these metallic elements apart by virtue of a dielectric layer. The cross resonator is a type of electric ring resonator (ERR) [5, 26] and couples strongly to uniform electric fields, and negligibly to magnetic fields. However, by paring the ERR with a metallic ground plane, the magnetic component of light couples to both the center section of the cross resonator and the ground plane, thus generating antiparallel currents resulting in resonant response. The magnetic response can therefore be tuned independent of the

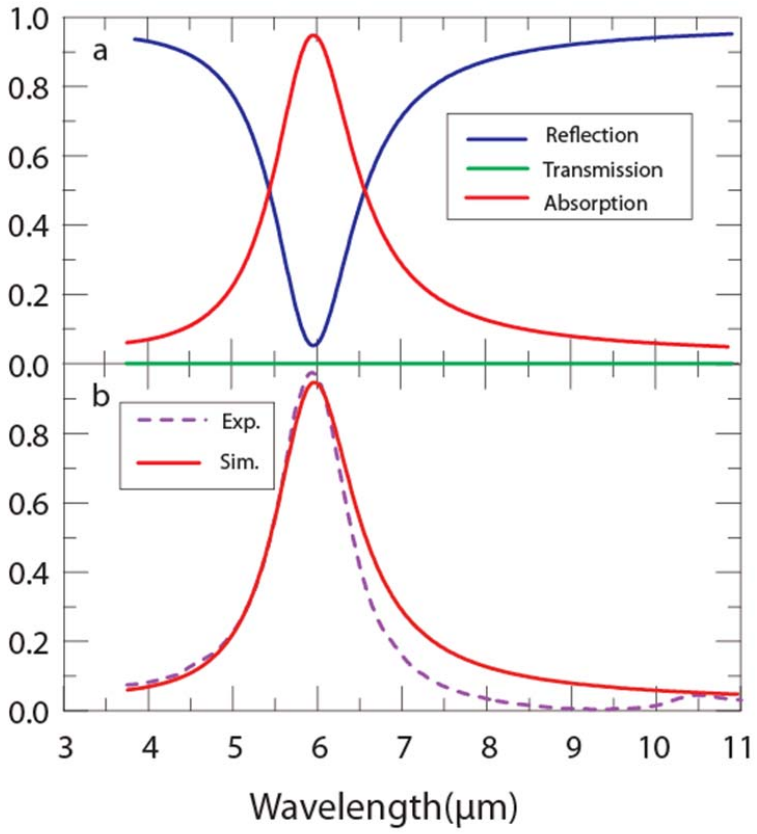

FIG. 2. Simulated and experimental performance of the infrared metamaterial absorber. (a) Numerical simulations of the electromagnetic response: Reflection (blue line), transmission (green line), and absorption (red line). The maximum absorption at 6 μm is

97%. (b) A comparison between the experimental absorption (red line) and simulated absorption (dashed gray line). Inset of (b) shows an optical microscope image of the fabricated spatially dependent metamaterial absorber.

electric, by changing the geometry of the ERR and the distance between elements. By tuning the amplitude and frequency location of the electric and magnetic resonances it is possible to match the impedance *Z (ω)* of the MPA to free space, thus minimizing the reflectance at a specific frequency. The metallic ground plane is thicker than the penetration depth of light in the IR range and thus transmission of the MPA is zero. These two conditions thus lead to narrow band high absorption.

The optimized structure presented in Fig. 1 was obtained through computer simulations using the commercial program CST Microwave Studio 2009. The time domain solver was utilized and metallic portions of the metamaterial absorber were modeled as gold using a Drude model with a plasma frequency $\omega_p = 2\pi \times 2175$ THz and collision frequency $\omega_c = 2\pi \times 6.5$ THz [27]. We use Al2O3 as the dielectric spacer and simulate the dielectric constant and loss tangent as 2.28 and 0.04, respectively. The transmission $T(\omega) = |S_{21}(\omega)|^2$ and reflection $R(\omega) = |S_{11}(\omega)|^2$ were obtained from S-parameter simulations with appropriate boundary conditions to approximate a TEM wave incident on the structure with both electric and magnetic field vectors lying in plane and the wave vector perpendicular. The frequency dependent absorption was calculated as $A(\omega) = 1 - R(\omega) - T(\omega)$ where, as expected for the present design, S21 is nearly zero across the entire frequency range due to the metallic ground plane. The optimized

structure, Fig. 1(a), achieves a simulated maximum absorption at 6:0 m and has the geometrical parameters (in microns) of a =2.0, l =1.7, w =0.4, t =0.185 and the thickness of both metallizations was 0.1 μm. The simulated *R (ω)*, *T (ω)*, and *A (ω)* are shown in Fig. 2(a).

Simulations indicate the feasibility of realizing an infrared MPA, and we now thus turn toward experimental demonstration. Fabrication begins with E-beam deposition of a 100

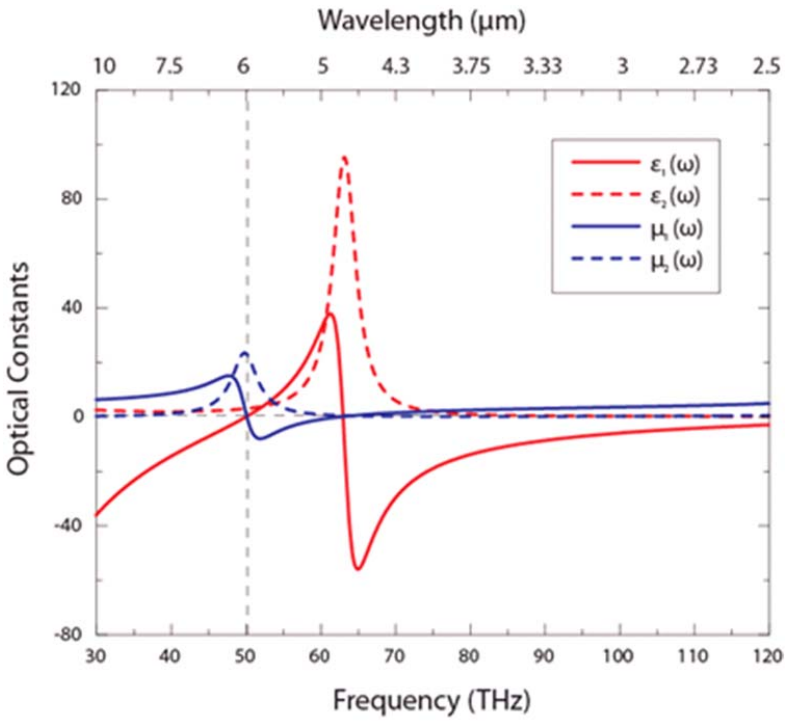

FIG. 3. Extracted optical constants for the simulated design.

nm thick layer of gold on a silicon substrate. This is followed by atomic layer deposition of a 185 nm thick layer of Al2O3. Resist 950 PMMA-A (MicroChem) was then spin coated on top and patterned using E-beam lithography. Another 100 nm thick layer of

gold was E-beam evaporated followed by liftoff in acetone. Figure 1(c) displays a scanning electron microscope (SEM) image of a single unit cell of the fabricated sample, and Fig. 1(d) shows a larger field of view. The total lateral size of the sample was 140 μm × 140 μm.

Transmission and reflection were characterized from a wavelength of 3–12 μm using a Fourier-transform infrared spectrometer combined with an infrared microscope (liquid-N2-cooled MCT detector, 15X cassegrain objective lens and KBr beam splitter). The reflection was measured at an incident angle of 20° and transmission was measured at normal incidence. The measured reflection spectra are normalized with respect to a gold mirror while the transmission spectrum is normalized with respect to an open aperture. The measured transmission and reflection are then used to calculate the absorption.

The experimental absorption is shown in Fig. 2(b) as the solid red curve. As shown in Fig. 2(a) the simulated transmission is effectively 0 across the entire range and a resonance occurs in the simulated reflectance at 6 μm where R = 0.03, thus yielding a maximum in the simulated absorption. The experimental absorption has a maximum at 6.0 μm with a value of 97%, with relatively low values to both lower and higher frequencies. The absorption has a full width half maximum of 1.0 μm and, at wavelengths of 4 and 10 μm $A(\omega)$, has fallen off to 10% and 1%, respectively. We achieve good agreement between experimental and simulated (dashed gray curve) absorptivities, as is evident from Fig. 2(b).

The optical constants were extracted for the present MPA design via inversion of the S parameters [28]. The retrieved [ε (ω)] and [μ (ω)] are displayed in Fig. 3, where the

vertical dashed line indicates the frequency (ω_0) of the absorption maximum (A_m). As can be observed, the real parts of the optical constants both cross zero at ω_0—as required for zero reflection. Note also that either ε_1 (ω) or μ_1 (ω) is always negative, i.e., when ε_1 (ω) > 0, μ_1 (ω) goes negative and vice versa. This is required for zero transmission across this range. By using the optical constants displayed in Fig. 3 we are able to recalculate R (ω), T (ω),, and A (ω),, not shown, thus verifying their validity. To further investigate the

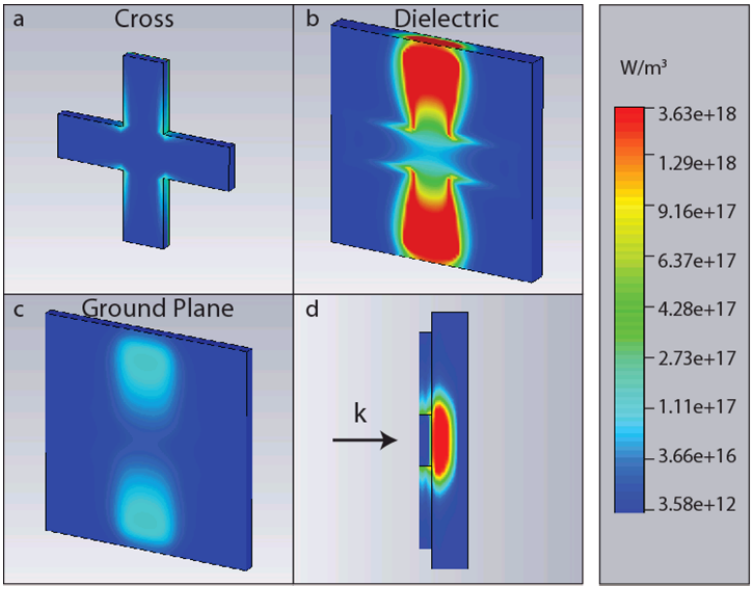

FIG. 4. Energy dissipation in the MPA structure at a wavelength of 6 µm. Energy dissipation distribution in (a) cross, (b) dielectric spacer, (c) ground plane, and (d) top view of the whole structure.

underlying absorption mechanism and to understand its various contributions, we computationally monitor energy dissipation in the MPA multilayer structure. The simulated energy loss is shown in Fig. 4 for each layer of the MPA [4(a)–4(c)] and for the structure as a whole [4(d)]. Simulations reveal that the majority of energy is dissipated as

dielectric loss within the Al2O3 layer and is an order of magnitude greater than the Ohmic loss within the metallic cross and ground plane.

In order to demonstrate the versatility of the MPA and its potential for applications, we combined our highly absorbing metamaterial, which we now term unit cell A (UCA), with an extremely low absorbing metamaterial, unit cell B (UCB). This is a type of metamaterial consisting of different sublattices, of which both bipartite [29] and tripartite [30] variations have been demonstrated. Unit cell B is of identical lateral proportions as UCA, i.e., 2 μm × 2 μm, and consists of the same metallic ground plane and Al2O3 dielectric with identical thicknesses. We use each of these two unit cells to form a pattern in the xy plane; i.e., we form a spatially selective or ‘‘graded’’ perfect absorber. The inset of Fig. 2(b) displays an optical microscope image of just such a design, forming the two letters ‘‘B’’ and ‘‘C.’’ The pattern of UCA consisted of 39 writing fields, each of dimensions 140 μm × 140 μm, where each contains nearly 5000 metamaterial unit cells. To avoid overlap we use a 4 μm space between neighboring UCA writing fields.

We characterized the graded metamaterial absorber using the same experimental setup as described earlier. A computer controlled linear stage moved automatically in the xy plane and we collected both R and T from wavelengths of 20 μm–600 nm. Reflection spectra are normalized with respect to an Au mirror with the same beam size. A spatial resolution of 50 μm was used, thus creating an image with 40 pixels along the x axis and 28 along the y axis. A total of 16 000 interferrogram points were collected for each pixel. A two-dimensional hyperspectral image is acquired, with a total data cube size of 1.8 ×

10^7, thus permitting investigation of both the frequency and spatial dependence of the sample.

We display 3D images of the data for a wavelength of 6 μm, shown in Figs. 5(a) and 5(b). The image is displayed as (x, y, A) and thus the x and y axes indicate the dimensions of the pattern and the z axis displays the absorption for each pixel. Clearly, as demonstrated in Fig. 5(a), at the resonance frequency of λ = 6 μm, the patterned metamaterial (unit cell A) achieves near-unity absorption. Figure 5(b) shows the x-z

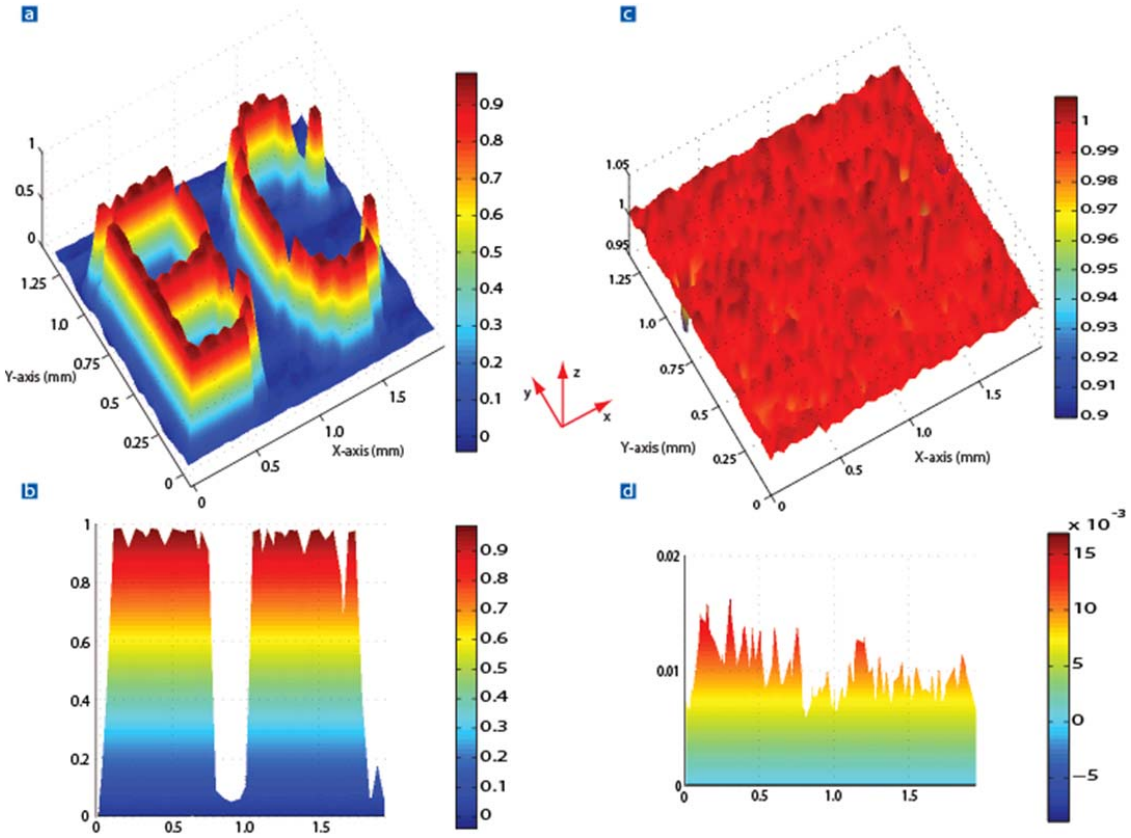

FIG. 5. Experimental three-dimensional images of the absorption and reflection of the graded metamaterial absorber. (a) Spatially dependent absorption image at a wavelength

of 6 μm (plotted to 100% absorption). (b) x-z view of the absorption at 6 μm. (c) Image of the reflection at a wavelength of 10 μm. (d) x-z view of the reflection at 10 μm.

plane from which it can be directly observed that absorption is near zero for UCB. Thus by using bipartite unit cells with perfect absorption and with near zero absorption, we have maximized contrast of the image.

In order to show the frequency dependence of the spatially selective MPA, in Figs. 5(c) and 5(d) we plot 3D images for a wavelength of $\lambda = 10$ μm. Data are in the form (x, y, R), where R is the reflectance, for Fig. 5(c) and (x, y, A) for Fig. 5(d). As can be observed, the reflectance is close to unity over the xy plane and, correspondingly, the absorption is near zero. A perfect metal at these wavelengths would give 100% reflectance and zero absorption. In contrast to both the optical photograph [Fig. 2(b)], and the image at 6 μm [Fig. 5(a)], at $\lambda = 10$ μm the MPA is not visible, i.e., indistinguishable from a perfect metal.

In conclusion, we have designed, fabricated, and characterized a midinfrared metamaterial perfect absorber, which achieves an experimental absorption of 97% at a wavelength of 6.0 μm. We further patterned the MPA to demonstrate the ability of achieving both a frequency and spatially selective absorption. Since one may specify a particular spatial pattern to be sent to a detector and the other component to be strongly absorbed, we have the ability to spatially modulate signals with large dynamic range. Dynamical range as large as 40 dB is achieved for our MPA without optimization, which is comparable to existing digital cameras [31]. These results suggest an alternative way to

achieve spatial light modulation, information coding, and single-pixel imaging. Interestingly, by combining the MPA with dynamical control [15, 16], the option of performing real-time subsample imaging, and hyperspectral subsample imaging, becomes possible. One advantage of dynamical metamaterials is that they may be fabricated with no moving parts [16]; i.e., they are all solid state. Because of the scalability of metamaterials, the concept of a spatially selective MPA suggests the ability of constructing SLMs which may operate at any subvisible frequency. The above listed advantages possible with metamaterials suggest exotic applications—in particular, hyperspectral single-pixel imaging cameras, which may alleviate the typically incurred trade-offs between cost, speed, signal-to-noise ratio, spectral resolution, and spatial resolution.

Bibliography

[1] V. G. Veselago, Sov. Phys. Usp. 10, 509 (1968).

[2] D. R. Smith et al., Science 305, 788 (2004).

[3] D. R. Smith et al., Phys. Rev. Lett. 84, 4184 (2000).

[4] R. A. Shelby et al., Science 292, 77 (2001).

[5] D. Schurig et al., Science 314, 977 (2006).

[6] J. B. Pendry, Phys. Rev. Lett. 85, 3966 (2000).

[7] N. Fang et al., Science 308, 534 (2005).

[8] N. I. Landy et al., Phys. Rev. Lett. 100, 207402 (2008).

[9] V. M. Shalaev et al., Opt. Lett. 30, 3356 (2005).

[10] S. Linden et al., Science 306, 1351 (2004).

[11] S. Zhang et al., Phys. Rev. Lett. 94, 037402 (2005).

[12] T. J. Yen et al., Science 303, 1494 (2004).

[13] M. Bayindir et al., Appl. Phys. Lett. 81, 120 (2002).

[14] M. C. K. Wiltshire et al., Science 291, 849 (2001).

[15] H.-T. Chen et al., Nat. Photon. 2, 295 (2008).

[16] H.-T. Chen et al., Nature (London) 444, 597 (2006).

[17] H.-T. Chen et al., Nat. Photon. 3, 148 (2009).

[18] H. Tao et al., Phys. Rev. B 78, 241103(R) (2008).

[19] H. Tao et al., Opt. Express 16, 7181 (2008).

[20] D. L. Donoho, IEEE Trans. Inf. Theory 52, 1289 (2006).

[21] E. J. Candes et al., IEEE Trans. Inf. Theory 52, 5406 (2006).

[22] E. J. Candes, in Proceedings of the International Congress of Mathematicians, Madrid, 2006 (European Mathematical Society, Madrid, 2006), Vol. 3, p. 1433.

[23] M. E. Gehm et al., Opt. Express 15, 14013 (2007).

[24] W. L. Chan et al., Appl. Phys. Lett. 93, 121105 (2008).

[25] W. L. Chan et al., Appl. Phys. Lett. 94, 213511 (2009).

[26] W. J. Padilla et al., Phys. Rev. B 75, 041102(R) (2007).

[27] M. A. Ordal et al., Appl. Opt. 22, 1099 (1983).

[28] D. R. Smith et al., Phys. Rev. B 65, 195104 (2002).

[29] Y. Yuan et al., Opt. Express 16, 9746 (2008).

[30] C. M. Bingham et al., Opt. Express 16, 18 565 (2008).

[31] S. Battiato et al., J. Electron. Imaging 12, 459 (2003).

Chapter 4

Taming the Blackbody with Infrared Me tamaterials as Selective Thermal Emitters

A blackbody is an idealized object that absorbs all radiation incident upon it and reradiates energy solely determined by its temperature, as described by Planck's law [1]. In reality no object behaves like an ideal blackbody; instead, the emitted radiation is determined by the absorption of the material. The desire to control radiated energy has long been a research topic of interest for scientists—one particular theme being the construction of a selective emitter whose thermal radiation is much narrower than that of a blackbody at the same temperature.

Various thermal emitters are desired for energy harvesting applications, such as in the field of thermophotovoltaics (TPVs), in that the conversion efficiently can be greatly enhanced. Extensive effort has been made using the luminescent bands of rare earth oxides for selective emission [2–4]. However such selective emitters are limited by the availability of materials and cannot be controlled beyond mixing various compounds, thus limiting their performance. Photonic crystals have been investigated as an alternative candidate for selective emitters [5–7]. However due to their nonresonant nature photonic crystal emitters do not have very sharp bands or high emissivity and therefore do not significantly increase efficiencies.

Another proposed technology which may be relevant for thermophotovoltaic applications is metamaterials [8–10]—artificial electromagnetic materials normally

composed of periodic metallic elements. Metamaterials have demonstrated the ability to achieve exotic properties difficult to attain with nature materials. One extraordinary property explored early on in metamaterials research is negative refractive index—theoretically predicted in 1968 [11] and experimentally demonstrated after 2000 [12–14].

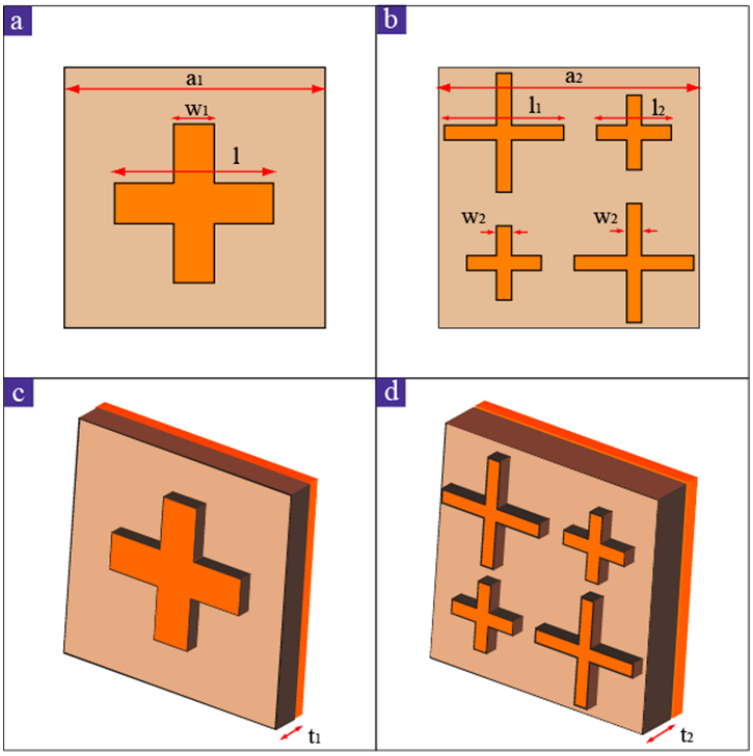

FIG. 1. Design of the infrared metamaterial absorber. (a) Top view of a single band metamaterial absorber unit cell with dimensions of: a = 3.2, l = 1.7, w_1 = 0:5, in microns. (b) Schematic of a dual-band metamaterial absorber with dimensions, (in microns): a2 = 7, l_1= 3.2, l_2 = 2.0, w2 = 0.4. (c) – (d) Perspective view for single and dual-band metamaterial absorbers. Thickness of dielectric spacer is: t_1 = 0.2 μm, t_2 = 0.3 μm.

Since then, research into metamaterials has grown enormously resulting in many novel phenomena including invisibility cloaks [15] and perfect lenses [16, 17]. An intriguing use of metamaterials has been development of the so called ‘‘perfect absorber’’, which exhibits the ability to yield near-unity absorptivity in nearly any frequency range [18–22]. According to Kirchhoff’s law of thermal radiation, at equilibrium the emissivity of a material equals its absorptivity. Therefore in principle, metamaterial perfect absorbers radiate energy as described by their absorptivity, at a given temperature. Because of the resonant nature of metamaterials the perfect absorber yields sharp resonances with high absorption, thus suggesting their use as high-Q emitters with high emissivity. Here we report on selective thermal emitters in the midinfrared range based on metamaterial perfect absorbers. We demonstrate that metamaterial emitters not only achieve high emissivity near the ideal blackbody limit, but are also capable of engineering the emissivity over large bandwidth in a desired wavelength dependent manner.

The unit cell of a single band infrared metamaterial absorber is shown in Fig. 1(a) and 1(c), and consists of two metallic elements; a cross shaped resonator and ground plane, with a dielectric layer spaced in between. Dimensions of the cross (in microns) are: a_1 = 3.2, l = 1.95, w = 0.5. The thickness of both metallizations is 0.1 μm and thickness of the dielectric spacer is 0.2 μm. This three layer metamaterial couples to both the electric and magnetic components of incident electromagnetic waves and allows for minimization of the reflectance, at a certain frequency, by impedance matching to free space [21]. The metallic ground plane is fabricated to be thick enough to prevent light transmission and therefore guarantees a narrow band absorber with high absorptivity. As the resonance

frequency of the cross resonator is proportional to its length, we may easily scale the above described design to longer or shorter wavelengths. We may also construct metamaterials consisting of different sublattices [23, 24], with different resonator lengths corresponding to different absorption bands. Based on this idea we combine two different metamaterial perfect absorbers to form a bipartite checker board unit cell, as shown in Fig. 1(b) and 1(d). The dimensions are, (in microns): a2 = 7, l_1 = 3.2, l_2 = 2:0, w_2 = 0.4. The thickness of metal layers in this dual-band absorber is 0.1 μm with a 0.3 μm dielectric layer in between.

Fabrication of the single band metamaterial absorber begins with e-beam deposition of a 0.1 μm gold layer on top of a silicon substrate. A layer of benzocyclobutene (BCB) is then spin coated and cured on top of the gold layer and is a final thickness of 0.3 μm. The top cross resonator is fabricated with deep UV lithography and a photo mask. The use of deep UV lithography permits fabrication of large surface areas and here we realize 300 mm (12 in) diameter samples where the fabricated metamaterial reticle has a total area of4 mm × 4 mm. The dual-band absorber is fabricated with e-beam lithography and, in this case, the dielectric spacer layer consists of Al2O3 deposited using atomic layer deposition (ALD) to a thickness of 0.2 μm. The total sample area of the dual-band absorber is about 4.5 m × 4.5 mm. Insets of Fig. 2(a) and 2(b) display SEM images of one unit cell for the fabricated single and dual-band absorber, respectively.

We first characterized the absorptivity A (ω) = 1- R (ω) - T (ω) for both the single and dual-band metamaterials. Measurement of the reflection and transmission is performed with a Fourier-transform infrared microscope. A liquid-N2-cooled MCT is used for

detection of radiation and is combined with a 15X cassegrain objective lens and KBr beam splitter. The reflection was measured at an incident angle of 20 degrees and transmission was measured at normal incidence. Reflection spectra are normalized with respect to a gold mirror and transmission with respect to an open aperture. The experimental absorptivity of the single band absorber is shown in Fig. 2(a), and Fig. 2(b)

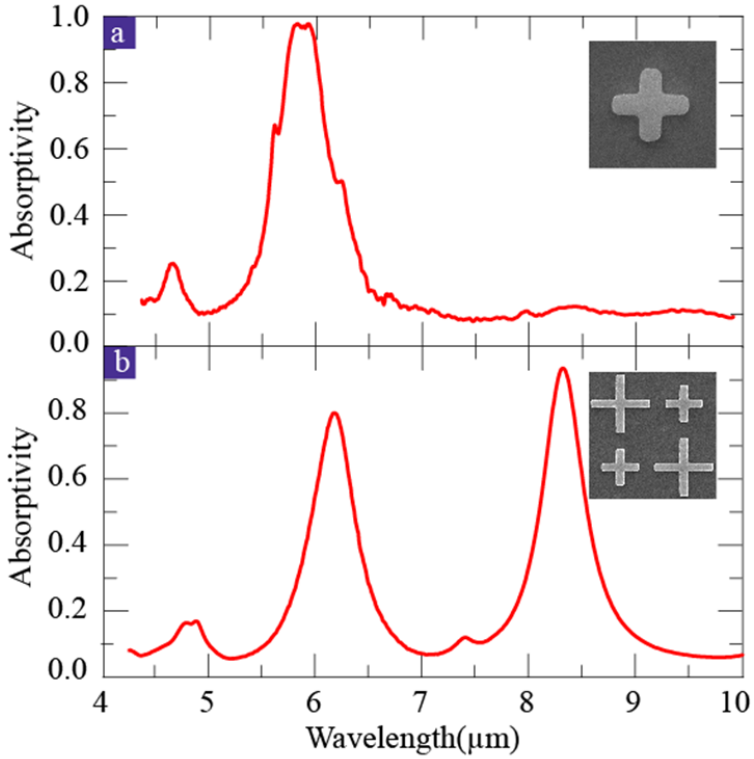

FIG. 2 (a) Experimental absoprptivity of the single band metamaterial absorber. (b) Experimental absoprptivity of the dual-band metamaterial absorber. Inset displays SEM images of one unit cell for the fabricated single and dual-band absorbers.

displays the absorptivity of the dual-band absorber. We can see from Fig. 2(a) and 2(b) that the single band absorber has an absorption peak at 5. 8 μm with 97% absorption and

two absorption bands can be observed for the dual-band absorber at 6.18 μm and 8.32 μm with 80% and 93.5% absorption, respectively.

Experimental results presented in Fig. 2 verify the ability of metamaterials for engineering absorption and we now turn toward experimental demonstration of tailored emissivity. An emission adaptor is attached to the external source port of the FT-IR

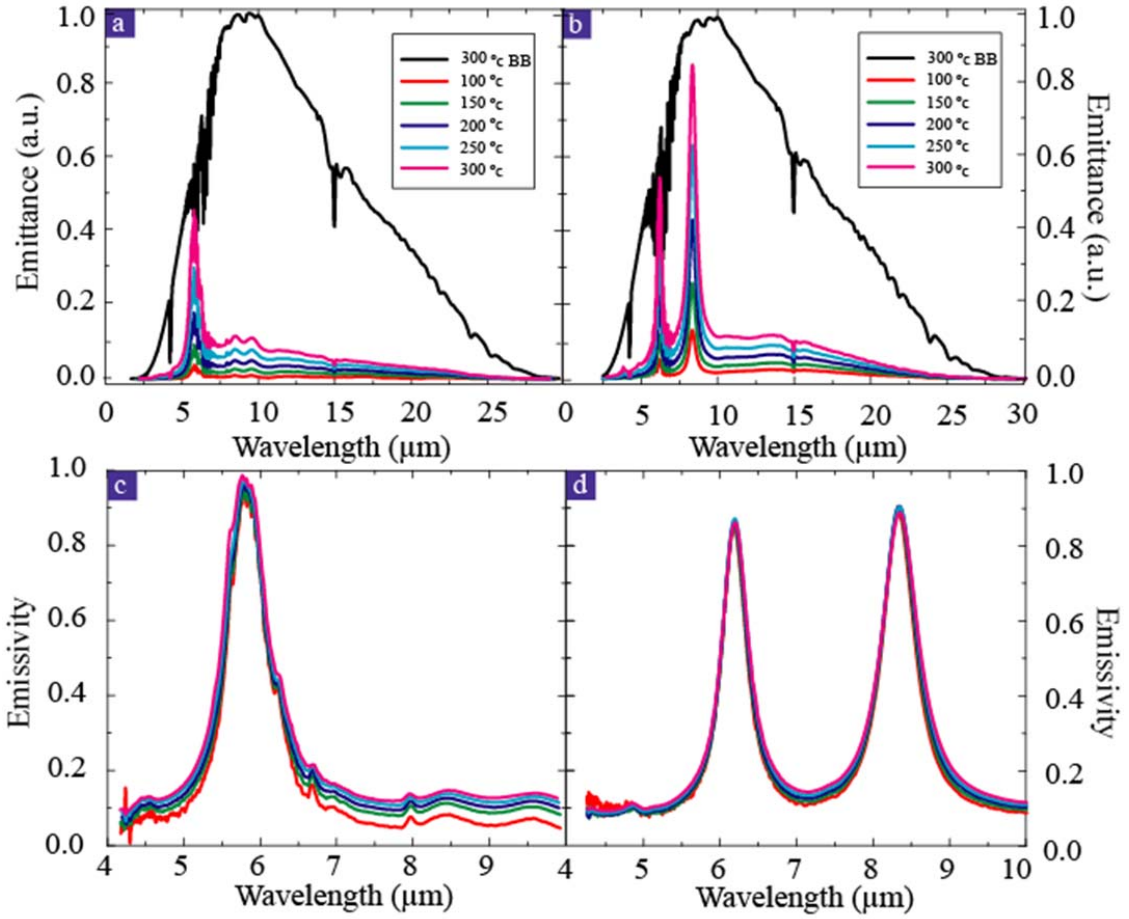

FIG. 3. Experimental emittance and normalized emissivity. (a) Emittance of the single band metamaterial emitter at five different temperatures and Emittance of the blackbody reference at 300 ºC. (b) Emittance of the dual-band metamaterial emitter at five different

temperatures and Emittance of the blackbody reference at 300 ºC. (c) Normalized emissivity of single band metamaterial emitter. (d) Normalized emissivity of dual-band metamaterial emitter.

system. A temperature controller permits emission studies from room temperature to 400 ºC in 1 degree steps. Radiation emitted from metamaterials is used as the source in the FT-IR spectrometer along with a KBr beam splitter and a DTGS detector. We characterize metamaterial emitters from 100 ºC to a maximum of 300 ºC in steps of 50 degrees.

In Figs. 3(a) and 3(b) we display the measured emittance of the single and dual-band metamaterial samples, respectively. For each a broad background is observed which increases for increasing temperature. Most notably, however, are sharp emittance peaks ranging from about 6 microns to just over 8 microns for both metamaterials. Our DTGS detector is not calibrated; thus, emittances shown in Fig. 3 are in arbitrary units. We can, however, characterize the absolute value emissivity through characterization of the temperature dependent emittance of a blackbody reference—black carbon. Displayed as the black curve in Fig. 3(a) and 3(b) is the blackbody reference emittance at 300 ————————————C. As can be observed, the emitted energy of the blackbody is significantly greater than that of the metamaterial emitters at the same temperature, except near 6 m for the single band, and near 6 and 8 μm for the dual-band sample, where metamaterial emissivities are nearly equal to that of the blackbody.

We may calculate the absolute value metamaterial emittance by division with the emittance of a perfect blackbody, (at the same temperature), thus providing the emissivity. The metamaterial temperature dependent emissivities are displayed in Fig. 3(c) and 3(d) for the single and dual-band emitters. The single band emitter yields relatively low values throughout the range displayed, but notably has an emission peak of 98% at 5:8 m. Similar behavior is observed for the dual-band emitter; i.e., it has a relatively low,

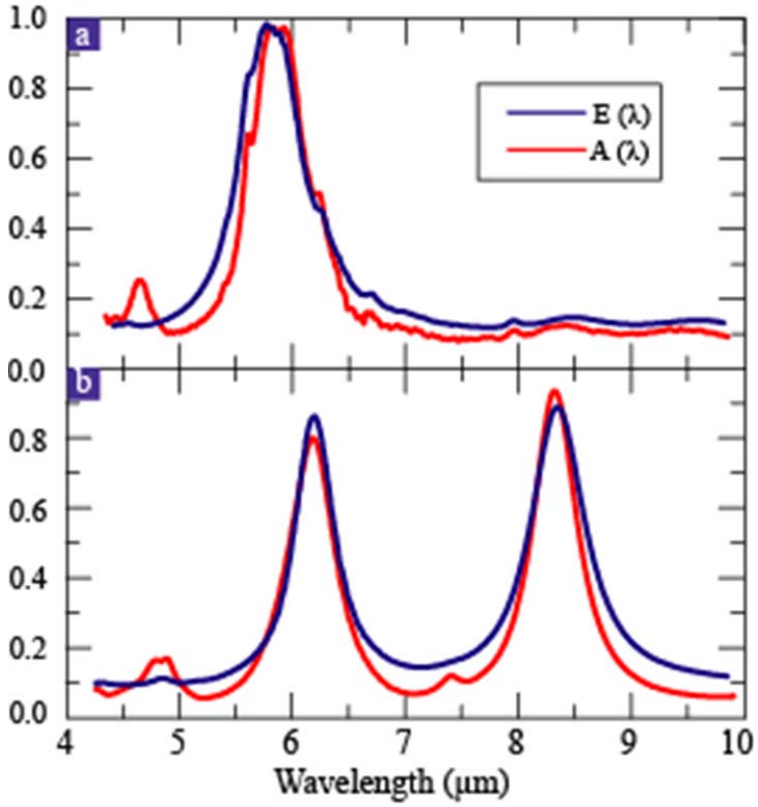

FIG. 4. Comparison between the experimental absorptivity and emissivity. (a) absorptivity and emissivity for the single band absorber (emitter). (b), absorptivity and emissivity for the dual-band absorber (emitter).

wavelength independent, emittance punctuated by two emission peaks of 85% and 89% at 6.18 and 8.32 μm, respectively. The emissivity for both emitters exhibits a bit of temperature dependence which we attribute to thermal expansion of the dielectric spacer layer [25, 26].

As a direct measure of utility of metamaterials to tailor emissivities, in Fig. 4 we compare the experimental absorptivity (red curves) and emissivity (blue curves) at 300 ºC, for both the single (a) and dual-band (b) emitters. According to Kirchoff's law of thermal radiation, at equilibrium these should be equal for all wavelengths, i.e. A (λ) = E (λ). Although the absorptivity is measured through transmission and reflection and the emissivity is characterized directly, we find good agreement between the two curves, as can be observed in Fig. 4. This verifies that the emissive properties of metamaterials can be tuned by the absorption, i.e., by modifying the transmissive and reflective properties.

As a final example of the extreme flexibility of metamaterials to provide engineered emissivities over a broad bandwidth, we computationally design a metamaterial for use with a thermophotovoltaic cell for energy harvesting applications. A TPV essentially converts radiated energy (usually infrared) to electrons, and consists of a thermal emitter and a photovoltaic cell. Efficiency of the TPV is governed by the Shockley-Queisser (SQ) limit, which is highly dependent upon the mismatch between incident photon energy and the band gap (EBG) of the semiconductor. One proposed method to increase TPV efficiency is to use selective emitters, whose emissivity is high within the TPV cell's sensitive region and low outside it. As a measure of the efficiency of TPVs we focus on the external quantum efficiency (EQE) which is the percentage of photons hitting the

semiconducting surface that will produce an electron-hole pair. As a specific example we use the EQE of a low energy semiconductor gallium antimonide (GaSb) [27]. Our goal is to design a metamaterial emittance which peaks at the bandgap energy of GaSb, is low for energies below EBG, and follows the EQE in a wavelength dependent manner for E>EBG.

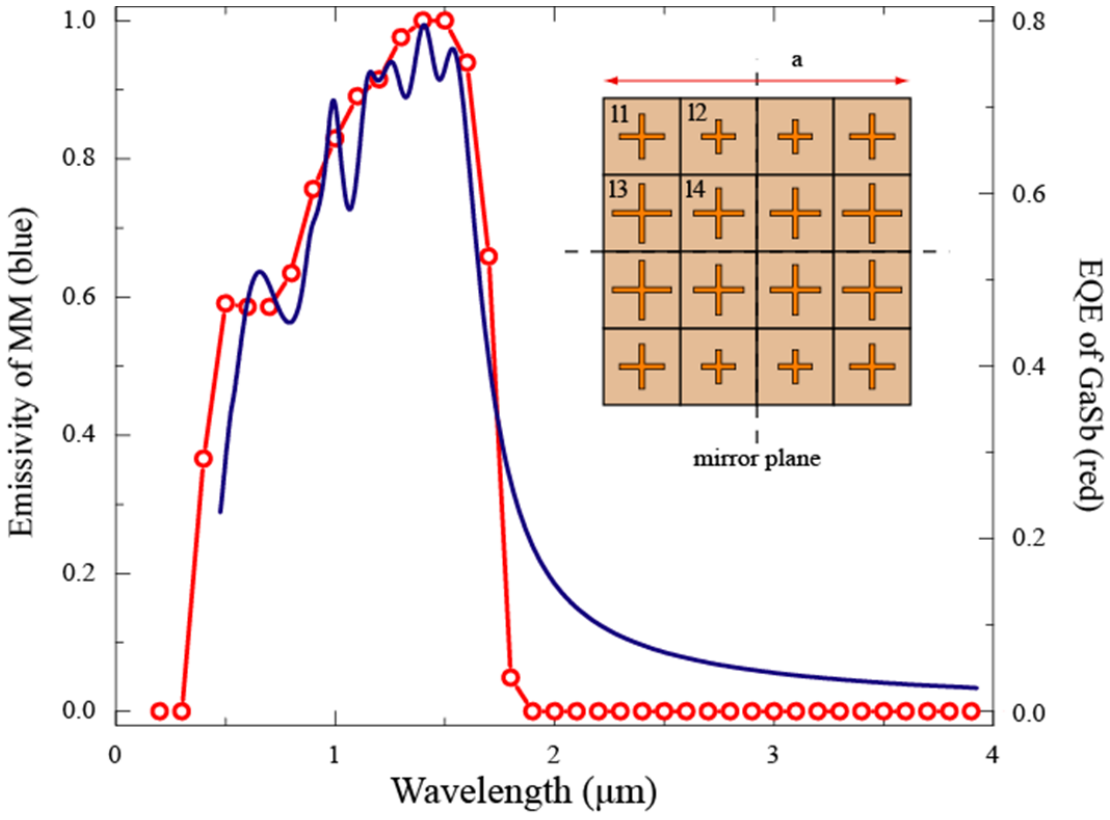

FIG. 5. Designed metamaterial emissivity (blue curve) and EQE (red curve) of GaSb. Inset shows a schematic of the metamaterial design with 16 sublattices. Dimensions of the design are a = 1080 nm, l_1 = 173 nm, l_2 = 127 nm, l3 = 221.5 nm, l4 = 190 nm. Each cross sublattice has a line width of 20 nm and thickness of 50 nm. The thickness of the

dielectric spacer is 78.8 nm and the ground plane is 200 nm. The unit cell also possesses two mirror planes, one horizontal and one vertical, as noted.

A metamaterial is computationally designed, following the same procedure previously outlined, and consists of a total of 16 sublattices with dimensions of l_1 = 173 nm, l_2 = 127 nm, l_3 = 221.5 nm, l_4 = 190 nm as shown in Fig. 5. The size of the unit cell with 16 sublattices is a = 1080 nm and each cross sublattice has a line width of 20 nm and thickness of 50 nm. The dielectric spacer used in the simulation is Al2O3 with thickness of 78.8 nm. Each sublattice consists of a cross resonator similar to those described for both the single and dual-band emitters. As in the case of the dual-band emitter, each sublattice independently achieves a designed emittance, both in terms of wavelength and amplitude. In this way we are able to engineer the emittance of the surface over a broad band, as shown in Fig. 5. Here we have designed the emittance to follow the EQE of GaSb in a wavelength dependent fashion. As can be observed metamaterials permit extreme engineering of the emissivity of surfaces.

We have experimentally realized single and dual-band metamaterial emitters. A comparison of emissivity to absorptivity shows good agreement, as predicted by Kirchoff's law of thermal radiation. Metamaterial emitters yield sharp bands (high Q) at infrared frequencies, peaking near the theoretical blackbody maximum. This suggests they are ideal candidates for energy harvesting applications. Other applications may benefit from the use of dynamical control [28–30], which may be implemented to provide tunable selective emitters which can be controlled by means of external stimuli. The

utilization of polymer spacing layers combined with deep UV lithography implies their possible use for applications which require flexible large area control of emittance. A further benefit of the metamaterial emitters described here is their ability to achieve broad bandwidth response by the utilization of more complex sublattice designs. Through manipulation of the structures, these bands can be independently controlled in both magnitude and wavelength, thus providing precise control of thermal radiation in nearly any desired manner. The scale independent nature of metamaterials further suggests the option of engineering emissivities in other relevant bands of the electromagnetic spectrum.

Bibliography

[1] M. Planck, Ann. Phys. (Leipzig) 309, 553 (1901).

[2] D. L. Chubb, A. M. T. Pal, M. O. Patton, and Jenkins, J. Eur. Ceram. Soc. 19, 2551 (1999).

[3] B. Bitnar, W. Durisch, J. -C. Mayor, H. Sigg, and H. R. Tschudi, Solar Energy Mater. Sol. Cells 73, 221 (2002).

[4] G. Torsello, M. Lomascolo, A. Licciulli, D. Diso, S. Tundo, and M. Mazzer, Nature Mater. 3, 632 (2004).

[5] M. U. Pralle et al., Appl. Phys. Lett. 81, 4685 (2002).

[6] S.Y. Lin, J. Moreno, and J. G. Fleming, Appl. Phys. Lett. 83, 380 (2003).

[7] M. Laroche, R. Carminati, and J.-J. Greffet, Phys. Rev. Lett. 96, 123903 (2006).

[8] C. Fu and Z. M. Zhang, Front. Energy Power Eng. China 3, 11 (2009).

[9] Y. Avitzour, Y.A. Urzhumov, and G. Shvets, Phys. Rev. B 79, 045131 (2009).

[10] W. J. Padilla, X. L. Liu, SPIE Newsroom (2010).

[11] V. G. Veselago, Sov. Phys. Usp. 10, 509 (1968).

[12] D. R. Smith, W. J. Padilla, D. C. Vier, S. C. Nemat-Nasser, and S. Schultz, Phys. Rev. Lett. 84, 4184 (2000).

[13] R. A. Shelby, D.R. Smith, and S. Schultz, Science 292, 77 (2001).

[14] D. R. Smith, J. B. Pendry, and M. C. K. Wiltshire, Science 305, 788 (2004).

[15] D. Schurig, J. J. Mock, B. J. Justice, S. A. Cummer, J. B. Pendry, A. F. Starr, and D. R. Smith, Science 314, 977 (2006).

[16] J. B. Pendry, Phys. Rev. Lett. 85, 3966 (2000).

[17] N. Fang, H. Lee, Ch. Sun, and X. Zhang, Science 308, 534 (2005).

[18] N. I. Landy, S. Sajuyigbe, J. J. Mock, D. R. Smith, and W. J. Padilla, Phys. Rev. Lett. 100, 207402 (2008).

[19] H. Tao, C. M. Bingham, A. C. Strikwerda, D. Pilon, D. Shrekenhamer, N. I. Landy, K. Fan, X. Zhang, W. J. Padilla, and R. D. Averitt, Phys. Rev. B 78, 241103(R) (2008).

[20] H. Tao, N. I. Landy, C.M. Bingham, X. Zhang, R. D. Averitt, and W. J. Padilla, Opt. Express 16, 7181 (2008).

[21] X. L. Liu, T. Starr, A. F. Starr, and W. J. Padilla, Phys. Rev. Lett. 104, 207403 (2010).

[22] J. M. Hao, J. Wang, X. L. Liu, W. J. Padilla, L. Zhou, and M. Qiu, Appl. Phys. Lett. 96, 251104 (2010).

[23] Y. Yuan et al., Opt. Express 16, 9746 (2008).

[24] C. M. Bingham et al., Opt. Express 16, 18 565 (2008).

[25] S. Guo, I. Lundstro¨m, and H. Arwin, Appl. Phys. Lett. 68, 1910 (1996).

[26] C. P. Wong and R. S. Bollampally, J. Appl. Polym. Sci. 74, 3396 (1999).

[27] O.V. Sulima, A.W. Bett, M. G. Mauk, Y. B. Ber, and P. S. Dutta, Proc. 5th TPV Conf., Rome, Italy, September 2002

(AIP, New York, 1999) p. 402.

[28] H.-T. Chen, J. F. O'Hara, A. K. Azad, A. J. Taylor, R.D.

Averitt, D. Shrekenhamer, and W. J. Padilla, Nat. Photon. 2, 295 (2008).

[29] H.-T. Chen, W. J. Padilla, J.M.O. Zide, A. C. Gossard,

A. J. Taylor, and R. D. Averitt, Nature (London) 444, 597 (2006).

[30] H.-T. Chen, W. J. Padilla, M. J. Cich, A. K. Azad, R. D. Averitt, and A. J. Taylor, Nat. Photon. 3, 148 (2009).

Chapter 5

Dynamic Manipulation of Infr ared Radiation with MEMS Metamaterials

The advent of metamaterials has ushered in a new era of designer electromagnetic materials and has realized novel responses ranging from negative refractive index [1-4] and superlensing [7] to perfect absorption [8, 9] and cloaking [5, 6]. Metamaterials are fashioned from 'artificial atoms,' which are engineered to yield a specific response to the electric and magnetic components of light – the properties of which are preserved in a macroscopic medium fabricated from their individual units. Electromagnetic properties achieved by metamaterials derive from the geometry of their unit cells, as opposed to the band-structure of their makeup. Metamaterials are thus a bottom-up design paradigm for the construction of advanced materials and hold great potential for applications spanning the electromagnetic spectrum. Although metamaterial have realized novel electromagnetic properties, some which have been difficult to achieve with natural materials, the ability to dynamically control these responses in real-time would offer significant advantages enabling metamaterials to transition into state-of-the-art devices.

Indeed in the past several years, tunable metamaterials have become an important development permitting real time tuning of various electromagnetic responses. Although much work has been carried out in the THz regime [11-17], and lower frequencies [18-20], there has been limited success in the infrared range [21]. Photo-excitation or electrical depletion of extrinsic carriers in semiconductor substrates has been proven to be

an effective way for achieving tunability at THz but is extremely difficult to achieve at shorter infrared wavelengths, which requires much higher doping densities thus leading to high currents and fields which tend to severely limit device lifetimes. Temperature controlled tunable metamaterial responses have been demonstrated in many frequency regimes [15, 16, 21, 22]; however the long response time prevents their practical use. Ferroelectric materials have been used to experimentally show tuning only at microwave frequencies [18], while liquid crystals [23, 24] may be implemented across many frequency bands.

Although metamaterials have demonstrated tuning by modification of substrate properties a viable alternative is to change the distance between the metamaterial elements, or the substrate, thereby altering the optimized resonant response and/or the local dielectric environment, thus providing tunability. Thus by fabricating metamaterials as microelectromechanical systems (MEMS) we may achieve mechanically actuated tuning [25-27]. In this communication we experimentally realize an electrically tunable MEMS metamaterial that effectively manipulates radiation in the mid-infrared wavelength range. The metamaterial consists of an array of suspended metal-dielectric elements above a metal ground plane on a carrier substrate. A voltage applied between the metallic metamaterial array and the bottom ground plane layer permits adjustment of the distance between them thus greatly altering the electromagnetic properties. The device functions in reflection mode and experimentally demonstrates infrared reflectivity with a modulation index of 56% at a wavelength of 6.2 m. Our device is compatible

with MEMS commercial foundries and can be incorporated with existing devices to achieve high speed infrared light modulation.

To date there have been several demonstrations of MEMS techniques utilized to achieve tunable response at THz and lower frequencies [28-31] and near infrared wavelengths [32] as well as for constructing diffractive gratings [33]. In our study, the

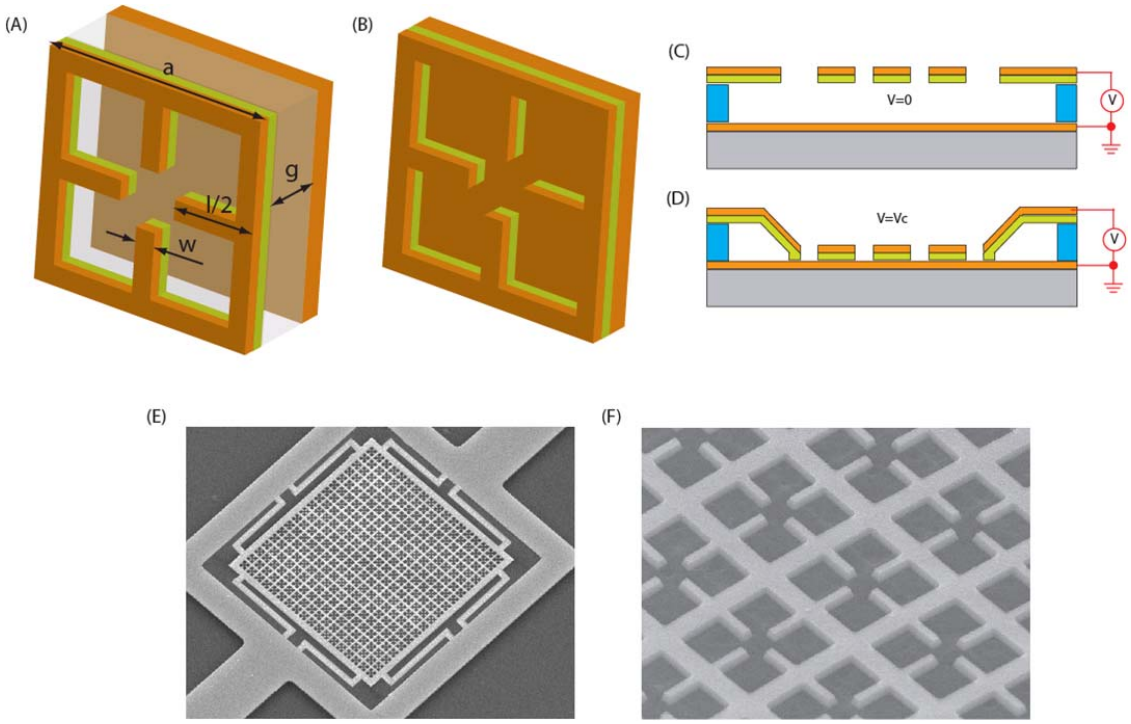

Figure 1. Schematic of a single unit cell of the tunable infrared metamaterial in the snap-back (A) and snap-down (B) states. The unit cell has the dimensions (in microns) of: a=3.5, l=2.6, w=0.4, g=1.2. The thicknesses of ground plane, dielectric layer and top metal layer are 200nm, 280nm and 100nm, respectively. The size of the metamaterial array (plus inner frame) is 65 x 65μm and consists of 18 x 18 unit cells. The linewidth of the spring arms is 2μm, the linewidth of the outermost frame is 10μm and the total device

is 100 x 100μm. (C) (D) Schematic demonstrating the tuning mechanism of the metamaterial device. (E) SEM image of the metamaterials device in perspective. (F) A close-up SEM image of the sample area.

metamaterial unit cell (shown in Fig. 1) consists of four layers above a carrier substrate. The top most metal layer is a Babinet metamaterial and is designed to yield an electrically resonant response [34, 35]. The Babinet metamaterial, and its underlying dielectric layer, are suspended on a supporting structure and are spaced above a ground plane – below which lies the carrier substrate. The ground plane is thicker than the penetration depth of light and thus our device is opaque to infrared radiation. Fig. 1, A and B shows the two states of the device which we term the "snap-down" and "snap-back" configurations. Our MEMS metamaterial has been designed to achieve a reflectivity minimum (highly absorbing configuration) in the snap-down state, i.e. under an applied bias, whereas in the snap-back state (no bias) the metallic-dielectric layer is suspended above the ground plane (with an air gap in-between) and a high reflectivity (low absorption) is intended. The mechanism of tunability, shown in Fig. 1, C and D, is through electrostatic force provided by application of a voltage bias between the top and bottom metallic layers. Details regarding the fabricational process are given in the supplementary materials. In Fig. 1 (E and F) we show SEM images of the fabricated sample which consists of the metamaterial array and eight cantilever arms (two arms per side lying around the perimeter) which provide a spring like restoring force thus enabling the device to be adjustable. As bias is applied to the top suspended metamaterial layer the

electrostatic force brings it closer to the ground plane. Notably, when the electrostatic force reaches a certain critical value, the suspended metallic-dielectric layer suddenly comes into contact with the underlying ground plane layer – a phenomenon known as

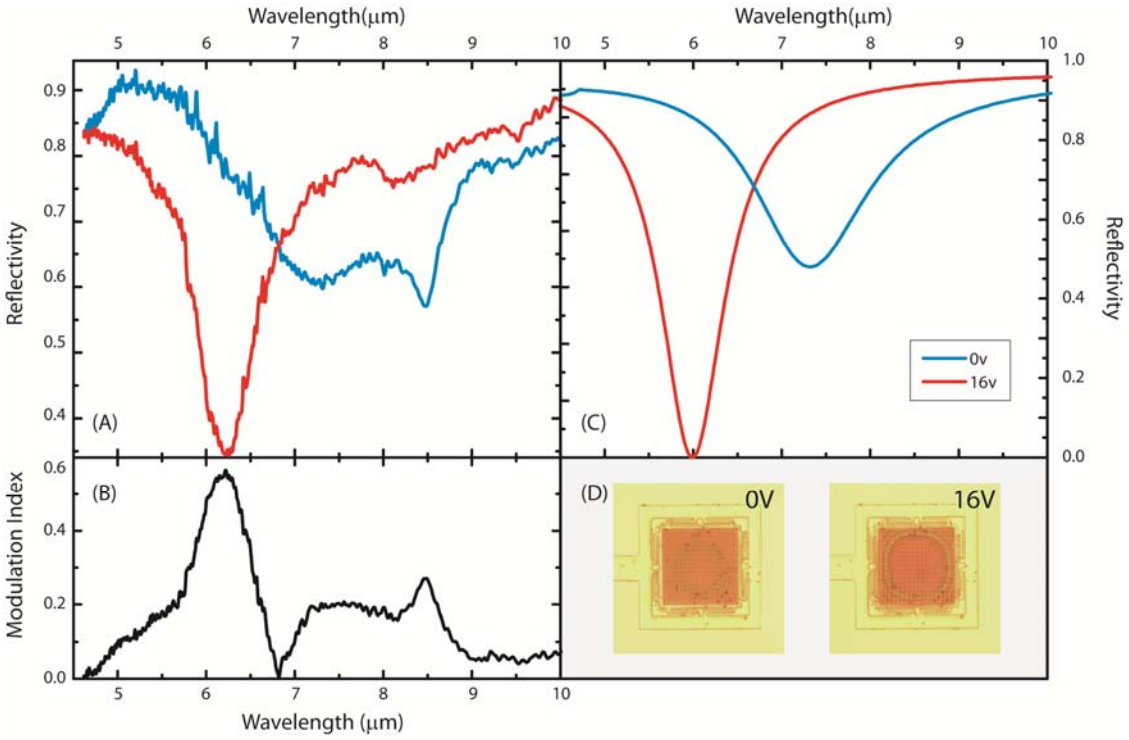

Figure 2. (A) Experimental reflectivity from the MEMS metamaterial in the snap-down (red curve) and snap-back (blue curve) configurations. (B) Modulation index as defined in the text. (C) Simulated reflectivity in the on and off states. (D) Optical images of the tunable metamaterial at 0 V (off – snap-back) and 16 V (on – snap-down) applied voltage.

snap-down [27]. After the applied voltage is removed, the cantilever arms restore the array to its initial suspended state.

The fabricated sample is characterized using an infrared microscope with a Fourier transform infrared (FTIR) spectrometer (see supplementary materials for details). We characterize the reflectivity from the sample with zero and various applied voltages – all referenced with respect to a gold mirror under identical conditions. Bias is then applied, increasing in 2 V increments, and we collect reflectivity spectra at each voltage. At the same time we continuously monitor the sample in the optical range with a microscope in order to detect any visible changes. We find that our MEMS metamaterial exhibits very little noticeable visible deformation until the applied voltage reaches 10 V, at which point snap-down occurs. At the snap-down voltage (V_{SD}) we notice that only the center area of the suspended array is in contact with the underlying ground plane. For increasing applied potential $V>V_{SD}$ we observe that the area of contact expands and we apply a maximum of V=16V. We then reduce the applied potential and collect reflectivity measurements – again in 2V increments. The real-time optical images obtained demonstrate that the contact area is continuously reduced until about 6 V, at which point our device snaps back to its original state. Optical images acquired at each voltage, and the corresponding electromagnetic response, are plotted in Fig.S3 of the supplementary materials. A real time movie of this process can also be found in the supplementary materials.

The experimental reflectivity is shown in Fig. 2(A) for both states, i.e. snap-down at 16V (red curve) and snap-back at 0V (blue curve). As previously mentioned our MEMS metamaterial has been designed to achieve a minimum in reflectivity (Rmin) in the snap-down configuration. As can be observed the reflectivity for 16V bias (red curves in Fig.

2(A)) is relatively high with values around 80-90%, except where the metamaterial achieves Rmin=34.5% at a wavelength of 6.2 μm. Fig. 2 D shows microscopic images of the tunable metamaterial at both 0 V and at 16 V. Our MEMS metamaterial in snap down mode achieves an impedance match to free space radiation and realizes a minimum in

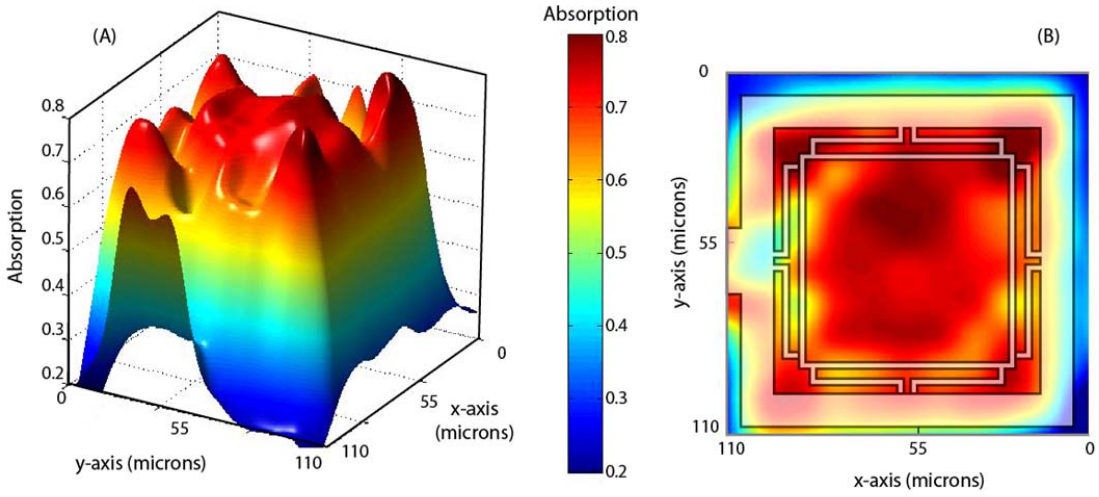

Figure 3. (A) Spatial dependence of the absorption across the surface of the MEMS metamaterial, shown as a false color three dimensional plot, in the snap-down state at a wavelength of 6.2 μm. (B) Contour of the corresponding 3D image shown in (A). The supporting frame for the metamaterial is shown as a transparent outline in (B) – metamaterial array lies within the innermost square frame. (Both images use the colormap shown to indicate absorption.)

reflection, and thus a maximum in absorption, since the transmission is zero. However when the layer is suspended (blue curve in Fig. 2(A)) above the ground plane, the

optimized impedance matched electromagnetic response of the metamaterial is broken, and the reflectivity achieves relatively high values, i.e. low absorption. Fig. 2 C displays the simulated reflectivity from the metamaterial (see supplementary materials for details). We find that simulations match well to the experimental reflectivity.

It is instructive to calculate the modulation index of our MEMS metamaterial device in order to quantify its potential performance as an infrared modulator. We define the modulation index as [36],"MI"=|R_max-R_min |/R_max where Rmax is the maximum reflectivity and Rmin is the minimum reflectivity. The modulation index is plotted in Fig. 2(B) and achieves a maximum of 56% at a wavelength of 6.2 μm, i.e. precisely where our metamaterial absorption is peaked. We also explored the ability of our infrared MEMS metamaterial to modulate at high speeds and found that our device may be operated in the kHz range and find a 3dB point of 30 kHz – see supplemental information for details.

The optical microscopic images presented in Fig. 2 (D), (and in Fig. S3 of the supplemental materials), reveal an interference pattern, similar to Newton's rings, which indicate that the metamaterial layer is not parallel to the underlying ground plane and is perhaps curved in nature. In order to explore the impact this bending has on the electromagnetic response, we perform infrared imaging of the surface of the MEMS metamaterial in the snap-down configuration – see Fig.3. We calculate the absorption as A=1-R and plot the three dimensional spatially dependent absorption in Fig. 3 (A) and a corresponding contour plot in Fig. 3(B), both on the same colorbar scale. The absorption can be observed to vary from approximately 80% to 55% across the metamaterial array.

This is consistent with the measured minimum reflection, i.e. Rmin=34.5% at 6.2 μm wavelength, shown as the red curve in Fig. 2A, which consists of the reflectivity averaged over the metamaterial array area.

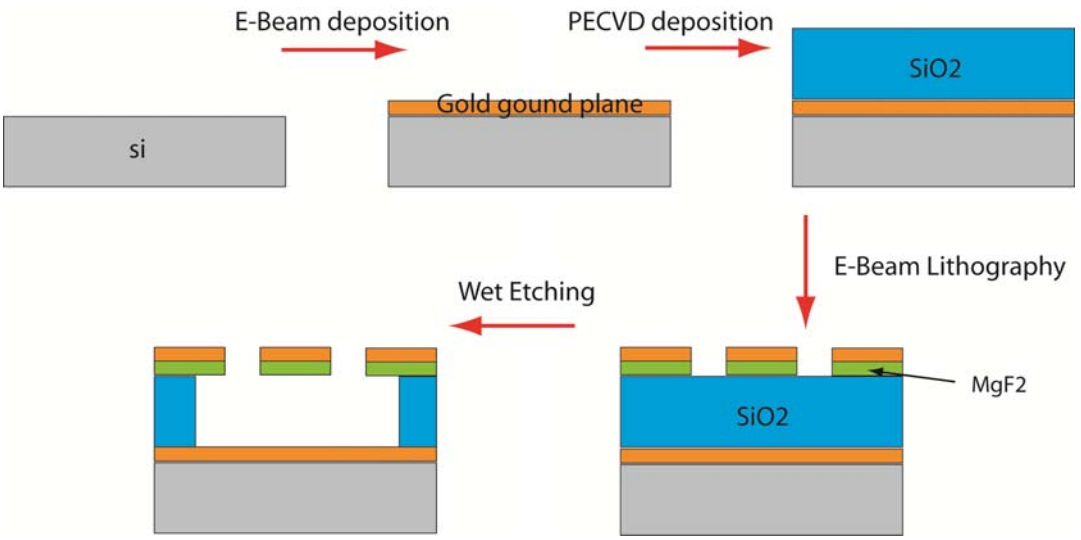

Figure. S1. Fabrication process for the infrared MEMS metamaterial.

Materials fabrication and characterization: Fabrication of the infrared MEMS metamaterial (Fig. 1) begins with depositing a layer of 200 nm thick gold on top of a silicon substrate using e-beam evaporation. A layer of 1.2 μm thick SiO2 is then grown on top utilizing PECVD. An e-beam resist is deposited and patterned then a 280 nm thick layer of MgF2 is added followed by e-beam evaporated 100 nm thick gold. After a lift-off process, the sample is immersed into a buffered oxide etching (BOE) solution for a critical time to remove the SiO2 below the metamaterial array but without fully removing the SiO2 below the surrounding frame. The end result is a suspended Gold-MgF2 metamaterial array suspended above a gold ground plane and supported by the SiO2

frame. The total area of the device is 100 μm by 100 μm with 20 μm wide exterior lines which connect to contact pads. The sample is mounted and wired to a sample holder to perform measurements. A detailed fabrication flow chart is shown in Fig. S1.

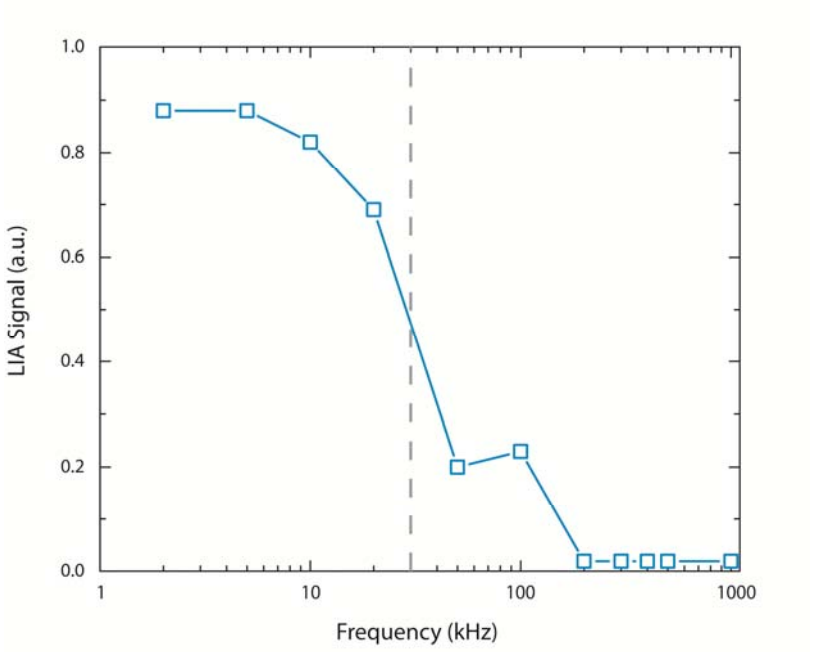

Figure. S2. Modulation signal as a function of bias frequency.

A Fourier-transform infrared spectrometer (FT-IR) combined with an infrared microscope is used to characterize the performance of the fabricated tunable metamaterial. In the experimental setup, we use a globar source, liquid-N2-cooled mercury cadmium telluride (MCT) detector and a potassium bromide (KBr) beam splitter. Reflection measurements are performed at an incident angle of 20 degrees and normalized with

respect to a gold mirror. The experimental transmission is found to be zero across the wavelength range of interest and is consistent with simulations.

Simulation: The structure presented in Fig. 1 is numerically simulated using the commercial program CST Microwave Studio 2012. The frequency domain solver is utilized and metallic portions of the metamaterial absorber are modeled as lossy gold. For the MgF2 dielectric material, we use a dielectric constant and loss tangent of 2.0 and 0.1,

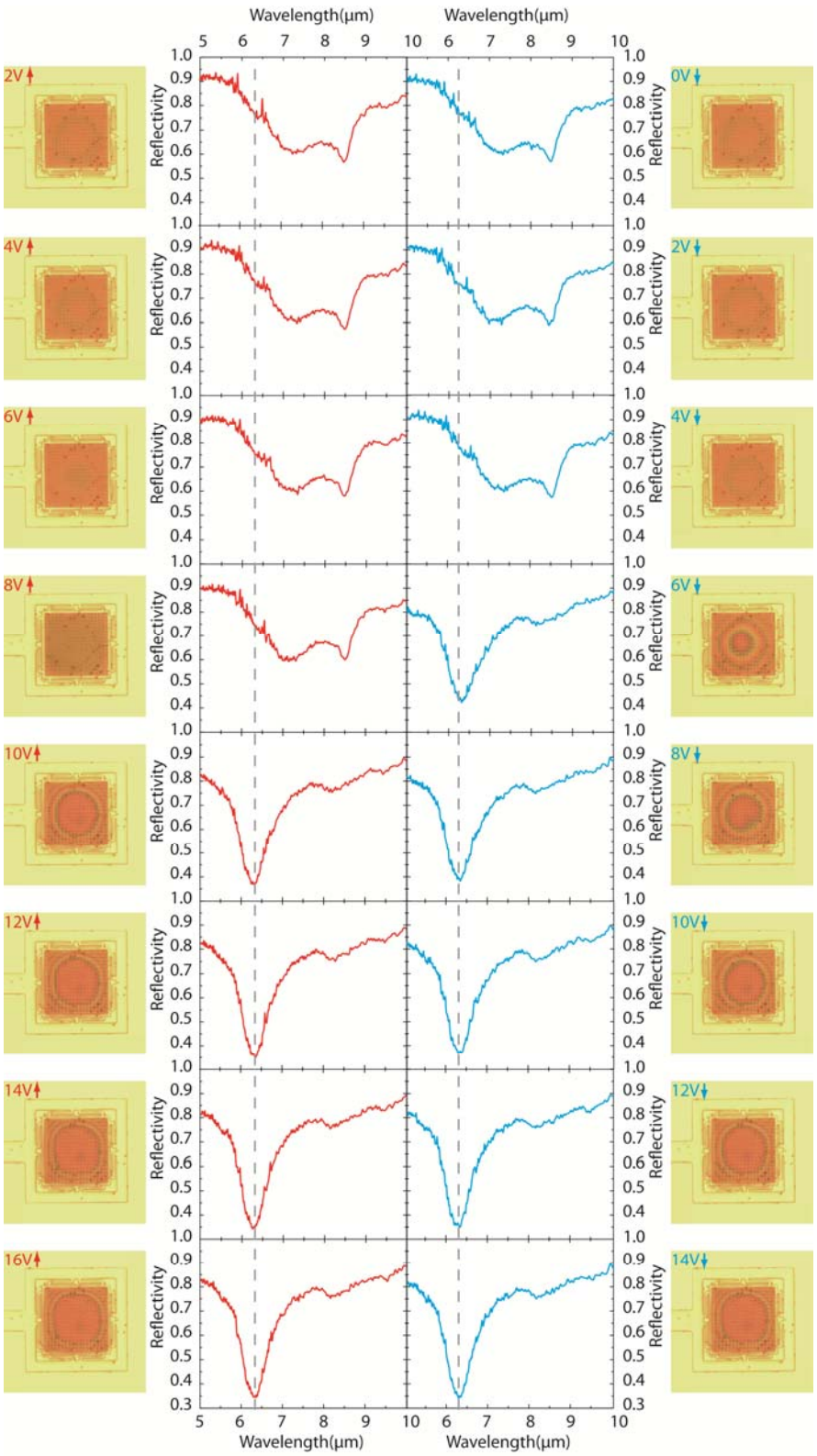
Wavelength(μm)
Wavelength(μm)
Reflectivity
2V
4V
6V
8V
10V
12V
14V
16V
0V
2V
4V
6V
8V
10V
12V
14V

Figure. S3. Optical images and their corresponding experimental reflectivity at each characterized applied bias for both increasing (left two panels – red curves) and decreasing voltage sweep (right panels – blue curves).

respectively. The reflectivity R is obtained from S-parameter simulations with appropriate boundary conditions to approximate a TEM wave incident on the structure with both electric and magnetic field vectors lying in plane and the wave vector perpendicular.

Modulation performance: The modulation speed defines how fast the tunable metamaterial device can be switched and is an important metric quantifying device performance. For practical applications, fast modulation speed is desirable. In order to determine the modulation speed of our tunable metamaterial, a function generator is used to provide a sine wave AC voltage (0-10 V) , which is applied to the two electrodes of the metamaterial device such that it functions as a fast oscillating modulator for the incident infrared beam in the FTIR-microscope setup. The modulated signal is output from the MCT detector into a lock-in amplifier (LIA) for signal characterization and a signal from the function generator provides a reference. We record the LIA signal value as a function of voltage frequency. We find a roughly constant LIA voltage signal which drops as we reach several tens of kilohertz. Fig.S2 shows the signal reading from LIA as function of input voltage frequency and we find that after 100 kHz the signal drops to zero. We find that the modulation speed of the tunable metamaterial is about 30 kHz – determined by the 3dB down point.

Further data analysis: To better understand the performance and tuning behavior of the infrared MEMS metamaterial, in Fig. S3 we plot the reflectivity data at each

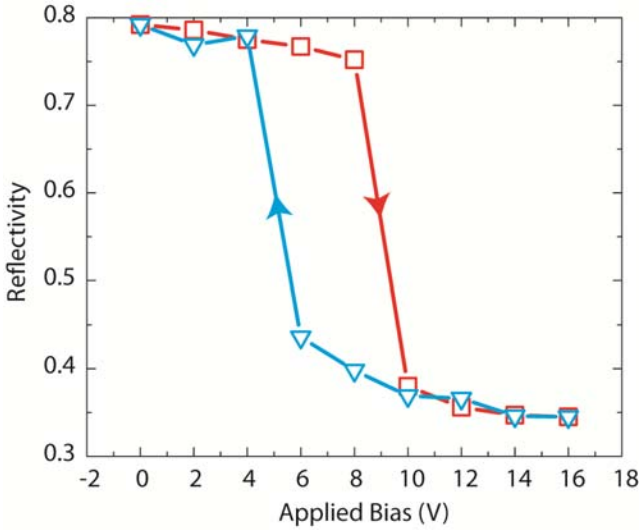

Figure. S4. Reflectivity at 6.2 μm as a function of applied voltage for increasing bias (red curve) and decreasing bias (blue curve). Reflectivity values are collected in 2V increments, as denoted by the square and triangular symbols.

characterized voltage for both increasing and decreasing sweeps. Next to each reflectivity plot we show an optical image of the sample for each corresponding voltage. As we can see from the optical images, when the applied voltage increases, the sample shows little change below VSD. When the applied voltage is near VSD, only the center area of the suspended array is in contact with the underlying ground plane and increasing applied potential V>VSD makes the area of contact expand. The decreasing voltage process shows a similar phenomenon in a reverse way. We trace the MEMS metamaterial resonance and Fig.S4 plots the reflectivity at 6.2 μm as a function of applied voltage for

both increasing and decreasing sweeps. The red curves represent the reflectivity for increasing applied voltages while the blue curves represent R for decreasing voltages. We can see from Fig. S4, the device achieves snap-down when the voltage reaches 10 V. However, upon the return voltage sweep, the MEMS metamaterial remains in snap-down until 6 V – characteristic of hysteresis due to charging.

The demonstration of the dynamic control of infrared radiation in reflection presented here provides a new path forward for the construction of exotic devices. By combining multiple metamaterial elements and, by utilizing individual tunability at each pixel, we may fashion spatial light modulators (SLMs) which enable manipulation of beam profiles in the mid-infrared range [37]. Infrared imaging could benefit from SLMs for the construction of single pixel hyperspectral imagers operating with various encoding schemes, such as compressive sensing [38], Hadamard imaging [39] and adaptive coded aperture imaging [40]. By operating our MEMS metamaterials at elevated temperatures our device also demonstrates the viability of fabricating surfaces which may be used to emit infrared radiation controlled in real-time across various bands, i.e. to construct infrared dynamic scene projectors [41]. Our structure is similar to the classical MEMS electrostatic actuator which realizes a life time on the order of billion cycles [42]. MEMS metamaterials shown here may also operate as direct detectors of infrared radiation. Incident energy is converted to heat within the metamaterial, as in bolometers, and thus combination with conventional infrared detecting materials, such as mercury cadmium telluride or thermal infrared cameras, would enable detection / imaging with spectral selectivity.

We have demonstrated a mechanically actuated metamaterial capable of high speed intensity modulation of infrared radiation in a reflection configuration. Full wave 3D simulations match well to experimental data and detail the mechanism of tunability. A modulation index of 56% at a wavelength of 6.2 μm was achieved and we have directly shown our device is capable of modulation speeds up to 30 kHz. Our designs may be readily scaled to other regions of the electromagnetic spectrum and are compatible with commercial MEMS foundries.

Bibliography

[1] V. G. Veselago, Sov. Phys. Usp. 1968, 10, 509.

[2] D. R. Smith, W. J. Padilla, D. C. Vier, S. C. Nemat-Nasser, S. Schultz, Phys. Rev. Lett. 2000, 84, 4184.

[3] R. A. Shelby, D. R. Smith, S. Schultz, Science 2001, 292, 77.

[4] D. R. Smith, J. B. Pendry, M. C. K. Wiltshire, Science 2004, 305, 788.

[5] D. Schurig, J. J. Mock, B. J. Justice, S. A. Cummer, J. B. Pendry, A. F. Starr, D. R. Smith, Science 2006, 314, 977.

[6] J. B. Pendry, Phys. Rev. Lett. 2000, 85, 3966.

[7] N. Fang, H. Lee, C. Sun, X. Zhang, Science 2005, 308, 534.

[8] N. I. Landy, S. Sajuyigbe, J. J. Mock, D. R. Smith, W. J. Padilla, Phys. Rev. Lett. 2008, 100, 207402.

[9] X. L. Liu, T. Starr, A. F. Starr, W. J. Padilla, Phys. Rev. Lett. 2010, 104, 207403.

[10] X. L. Liu, T. Tyler, T. Starr, A. F. Starr, N. M. Jokerst, W. J. Padilla, Phys. Rev. Lett. 2010, 104, 207403.

[11] W. J. Padilla, A. J. Taylor, C. Highstrete, M. Lee, R. D. Averitt, Phys. Rev. Lett. 2006, 96, 107401.

[12] H.-T. Chen, W. J. Padilla, J.M.O. Zide, A.C. Gossard, A.J. Taylor, R.D. Averitt, Nature 2006, 444, 597.

[13] H.-T. Chen, , J. F. O'Hara, A. K. Azad, A. J. Taylor, R. D. Averitt, D. B. Shrekenhamer, W. J. Padilla, Nature Photon. 2008, 2, 295.

[14] H.-T. Chen, W. J. Padilla, M. J. Cich, A. K. Azad, R. D. Averitt, A. J. Taylor, Nature Photon. 2009, 3, 148.

[15] T. Driscoll, H.-T. Kim, B.-G. Chae, B.-J. Kim, Y.-W. Lee, N. M. Jokerst, S. Palit, D. R. Smith, M. Di Ventra, D. N. Basov, Science. 2009, 325, 1518.

[16] H. Tao, A. C. Strikwerda, K. Fan, W. J. Padilla, X. Zhang, R. D. Averitt. Phys. Rev. Lett. 2009, 103, 147401.

[17] D. Shrekenhamer, S. Rout, A. C. Strikwerda, C. Bingham, R. D. Averitt, S. Sonkusale, and W. J. Padilla Opt. Express 2011, 19, 9968.

[18] T. H. Hand, S. A. Cummer, J. Appl. Phys. 2008, 103, 066105.

[19] D. Wang, L. Ran, H. Chen, M. Mu, J. A. Kong, B.-I. Wu, Appl. Phys. Lett. 2007, 91, 164101.

[20] M. Lapine, D. Powell1, M. Gorkunov, I. Shadrivov, R. Marqués, Y. Kivshar, Appl. Phys. Lett. 2009, 95, 084105.

[21] T. Driscoll, S. Palit, M. M. Qazilbash, M. Brehm, F. Keilmann, B.-G. Chae, S.-J. Yun, H.-T. Kim, S. Y. Cho, N. M. Jokerst, D. R. Smith, D. N. Basov, Appl. Phys. Lett. 2008, 93, 024101.

[22] M. J. Dicken, K. Aydin, I. M. Pryce, L. A. Sweatlock, E. M. Boyd, S. Walavalkar, J. Ma, H. A. Atwater, Opt. Express 2009, 17, 18330.

[23] D. H. Werner, D.-H. Kwon, I.-C. Khoo, A. V. Kildishev, V. M. Shalaev, Opt. Express. 2007, 15, 3342.

[24] David Shrekenhamer, Wen-Chen Chen, and Willie J. Padilla Phys. Rev. Lett. 110, 177403

[25] G. M. Rebeiz, RF MEMS: theory, design and technology, John Wiley & Sons, 2003

[26]A. Richter, and G. Paschew, Adv. Mater. 2009, 21, 979.

[27] J. S. Milne, J. M. Dell, A. J. Keating, and L. Faraone, Journal of Microelectromechanical Systems, 2009, 18, 4.

[28] W. M. Zhu, A. Q. Liu, X. M. Zhang, D. P. Tsai, T. Bourouina, J. H. Teng, X. H. Zhang, H. C. Guo, H. Tanoto, T. Mei, G. Q. Lo, D. L. Kwong, Adv. Mater. 2011, 23, 1792.

[29] Y. H. Fu, A. Q. Liu, W. M. Zhu, X. M. Zhang, D. P. Tsai, J. B. Zhang, T. Mei, J. F. Tao, H. C. Guo, X. H. Zhang, J. H. Teng, N. I. Zheludev, G. Q. Lo, D. L. Kwong, Adv. Mater. 2011, 21, 3589.

[30] F. Hu, Y. Qian, Z. Li, J. Niu, K. Nie, X. Xiong, W. Zhang and Z. Peng, J. Opt. 2013, 15, 055101.

[31] E. Ekmekci, K. Topalli, T. Akin and G. Turhan-Sayan, Optics Express, 2009, 17, 16046

[32] J.-Y. Ou, E. Plum1, J. Zhang and N. I. Zheludev, Nature Nanotechnology, 2013, 8, 252.

[33] J. L.Skinner, A. A. Talin, D. A. Horsley, Opt. Express. 2008, 16, 3701.

[34] W. J. Padilla, M. T. Aronsson, C. Highstrete, Mark Lee , A. J. Taylor, and R. D. Averitt, Phys. Rev. B, 2007, 75, 041102.

[35] H.-T. Chen, J. F. O'Hara, A. J. Taylor, R. D. Averitt, C. Highstrete, M. Lee, and W. J. Padilla, Optics Express, 2007, 15, 1084.

[36] M. Rahm, J.-S. Li, and W. J. Padilla, J Infrared Milli Terahz Waves, 2013, 34, 1.

[37] W. L. Chan, H. T. Chen, A. J. Taylor, I. Brener, M. J. Cich, and D. M. Mittleman, Appl. Phys. Lett. 2009, 94, 213511.

[38] D. L. Donoho, IEEE Trans. Inf. Theory 2006, 52, 1289.

[39] W. K. Pratt, J. Kane, and H. C. Andrews, Proc. IEEE 1969, 57, 58.

[40] C. Slinger, M. Eismann, N. Gordon, K. Lewis, G. McDonald, M. McNie, D. Payne, K. Ridley, M. Strens, G. De Villiers, and R. Wilson, Proc. SPIE 2007, 6714, 671408.

[41] O.M. Williams, Infrared Physics and Technology, 1998, 39, 473.

[42] R. Chan, R. Lesnick, David Becher, and M. Feng, J. Microelectromech. Syst. 2003, 12, 713.

Chapter 6

Metamaterials on parylene thin film substrates: Design, fabrication, and characterization at terahertz frequency

Parylene, discovered in the middle of past century, is the generic name of a family of polymers that has 20 variants, yet only three of them are most commonly used, Parylene N, C, and D.1 Due to its excellent mechanical, physical, electrical, and barrier properties, parylene is widely used in many areas, such as nanotechnology, electronics, medical, and pharmacopoeia industries [2, 3]. Industry applications typically use a chemical vapor deposition technique in order to form a parylene layer, with thicknesses ranging from hundreds of angstroms to several millimeters [4]. The advantage of this process is that the coating forms from a gaseous monomer without an intermediate liquid stage. Unlike liquid coatings, this technique ensures the parylene completely penetrates all crevices and uniformly coats surfaces such as sharp points, cavities, edges, corners, and micro/nanoscopic pores. The thin film is conformal for almost every exposed surface and is pinhole-free [5]. Parylene-C is deposited at room temperature and is compatible with micro-electro-mechanical systems (MEMS) technology processes. And it can also be readily separated from the substrates after the completion of device fabrication. Parylene films are chemically and biologically inert, very stable, and nearly unaffected by most acids, alkalines, or organic solvents. Another striking property of parylene films is that it is biocompatible and biostable which enable its wide use in medical areas such as implantable devices [6]. Other applications which benefits from parylene's excellent

properties include the following: circuit boards [7], ultrasonic applications [8], and surgical devices [9], Parylene has excellent dielectric properties as follows: low dielectric constant, low loss, and high dielectric strength, even in the form of very thin films [10]. These excellent properties stem from the fact that the film is conformal and free of defects, and suggest the use of parylene as a substrate material for electromagnetic metamaterials operating within the terahertz (TH) range.

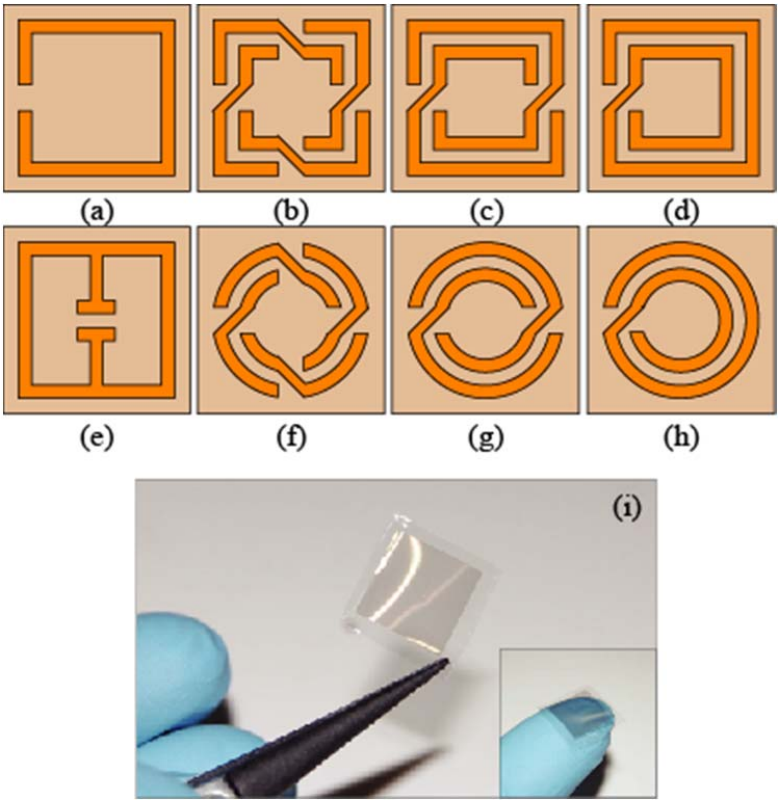

FIG. 1. (a)–(h) Schematic of the various metamaterials fabricated and characterized on parylene thin film substrates. The size of each unit cell is 100 × 100 μm^2. The outer dimension of each metamaterial is 72 × 72 μm^2 and the line width is 8 μm. All the gaps are 8 μm wide. For the spiral structures, the gap between inner and outer metal is 4 μm. (i) Photographs of metamaterials on parylene thin film substrate.

Electromagnetic metamaterials, artificial materials made from structured composites, have attracted much attention from the scientific community after experimental demonstration of negative index of refraction in 2000 [11]. Other striking examples and blooming areas of metamaterial research includes super lenses [12] and invisible cloaks [13]. It is predicted that numerous applications will thrive within the THz frequency range. Metamaterials operating in the THz range have had great successes in filling in the so-called "electromagnetic gap," lying between microwave and infrared frequencies. Some metamaterials devices have been demonstrated such as modulators, filters, and perfect absorbers [14]. Perfect absorbers have been reported as an imaging tool at THz frequencies and may have application in biomedical diagnostic areas such as skin cancer detection [15]. The use of parylene as a substrate or coating for metamaterials is further motivated by the fact that many diagnostic detectors are implanted directly into the human body. Materials which constitute the detector should be stable and compatible with human body—one of the salient features of parylene films. In this letter, we demonstrate that metamaterials fabricated on parylene thin film substrates have strong resonances at THz frequencies with low loss. This verifies the potential usage of parylene as metamaterial coatings or substrates for bioimplanting applications within the human body.

We designed and fabricated several types of metamaterials, as show in Fig. 1. Some of these, such as the canonical split ring resonator (SRR) and the electrical ring resonator, are well characterized at THz frequencies, shown in Figs. 1(a) and 1(e), respectively. A

silicon wafer was used as a platform for fabrication. After dehydration baking the wafers at 150 °C, ten micron thick film of parylene-C was deposited using a Labcoter 2 Parylene Deposition Unit (Specialty Coating Systems, Indianapolis, IN). The dimer charge was vaporized at 175 °C and 1 Torr, decomposed to its monomer (paraxylylene) at 690 °C and 0.5 Torr, and deposited on the wafers at 25 °C and 0.1 Torr. The metamaterials were next created utilizing a photoresist (AZ nLOF 2020) using conventional photolithography. Then, a 10 nm/200 nm thick Ti/Au layer was sputter deposited onto the parylene-C. Next, we performed lift-off by placing the wafer in an acetone bath. Finally, the parylene-C substrate containing metamaterial structures were peeled off the silicon wafer, shown in Fig. 1(i).

We simulated the electromagnetic response of the metamaterials using the commercial FDTD program Microwave Studio. Dimensions were modeled as according to Fig.1. Perfect electric and perfect magnetic boundary conditions are used to polarize the electric and magnetic field components, vertically and horizontally with respect to Fig. 1. Ports were use on the remaining two boundaries to simulate a plane wave incident on the metamaterial. The transient solver is used to obtain the complex S-parameters.

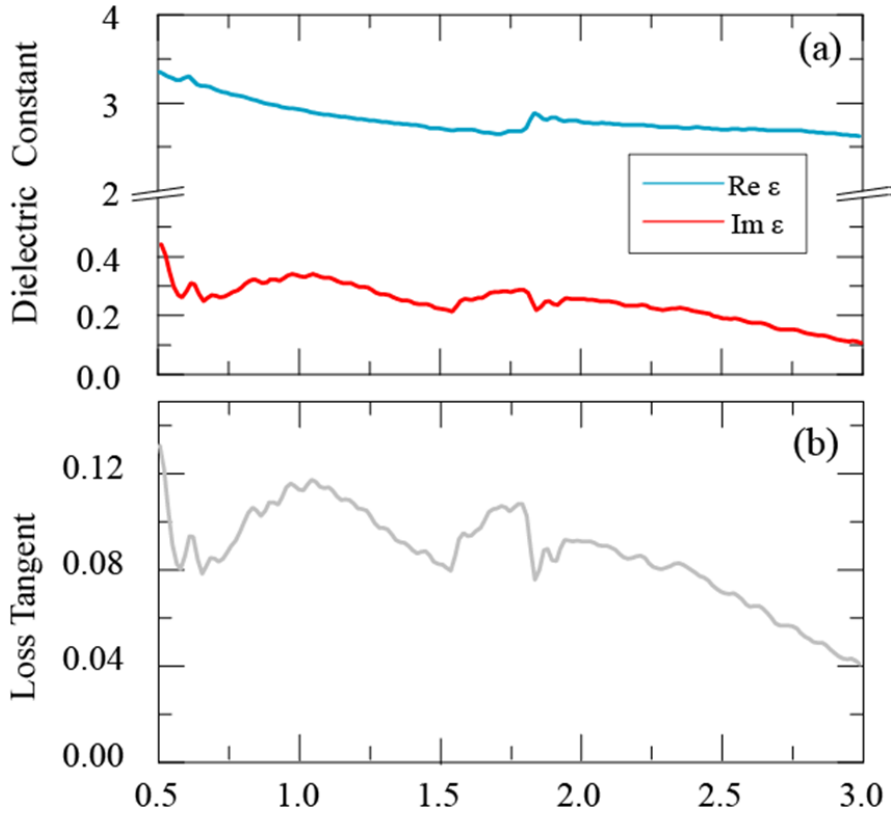

FIG. 2. (a) Dielectric constant and (b) Loss tangent of 20 μm thickness parylene thin film.

The metamaterial/parylene samples were characterized using a Fourier-transform infrared (FTIR) spectrometer. A liquid-helium-cooled Si bolometer is used as a detector and an Hg arc lamp as the source. A polarizer is used to obtain the desired electric field orientation. We use both a 50 μm thick mylar and germanium coated 6 μm thick mylar beam splitter to cover the desired frequency range. The samples were mounted at normal incidence for transmission measurements and 30° incidence from normal for the reflection measurements.

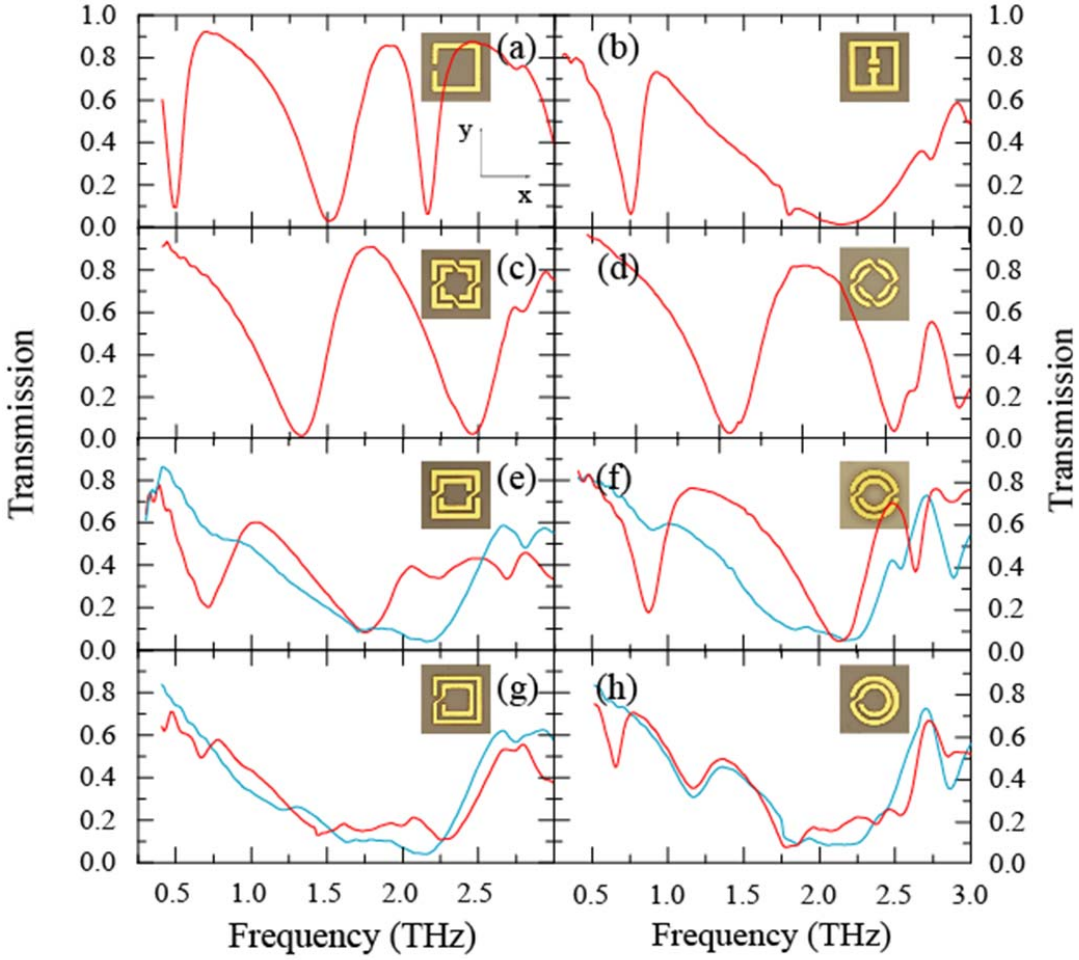

FIG. 3. Transmission spectrum for metamaterials on parylene thin film. The red curves represent electric field polarized along y direction and the blue ones are for x polarization. Insets are the optical microscopic images or corresponding metamaterials.

We also characterized the complex dielectric properties [$\varepsilon(\omega) = \varepsilon_1 + i\varepsilon_2$] of parylene thin films using the FTIR. Both the transmission T (ω) and reflection R (ω) were measured for a 20 μm thick parylene free standing film. We make an approximation in this system; treating the parylene permeability equal to the free space value. T (ω) and R

(ω) were then inverted using the Levenberg–Marquardt algorithm to numerically solve for the frequency dependent complex dielectric function for the parylene thin film.16 In the program code we assume normal incidence reflection which does not significantly affect the results. We extracted both the real ε_1 and imaginary part ε_2 of the dielectric constant and calculated the loss tangent of the parylene film, as shown in Figs. 2(a) and 2(b), respectively. The result clearly shows that parylene thin films are a low loss material within the THz frequency range, and thus make a good substrate material for potential applications.

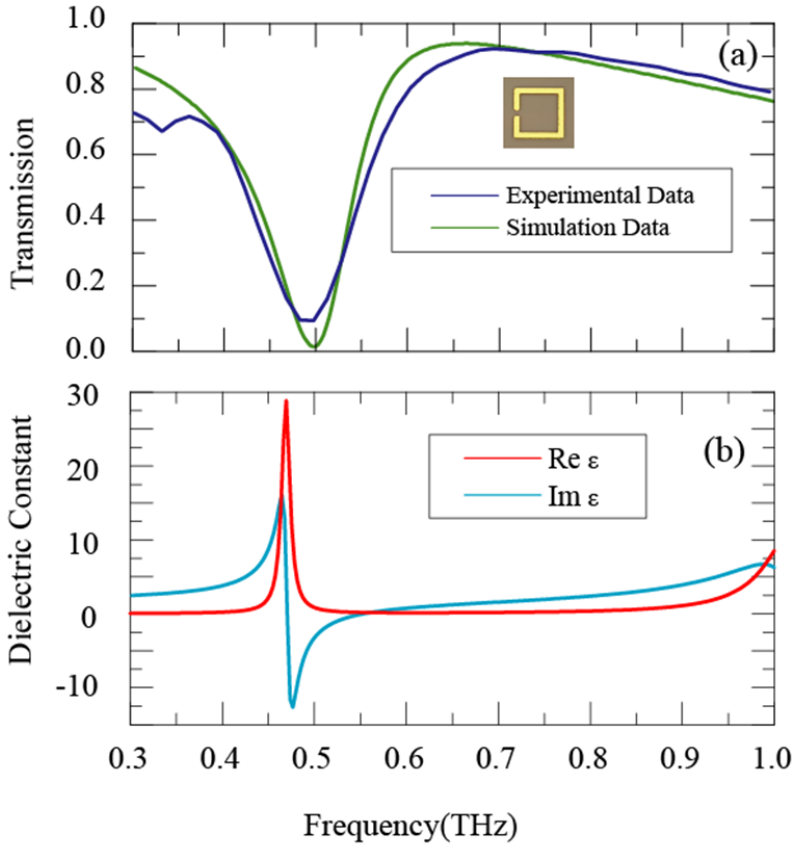

FIG. 4. (a) Comparison of simulation and experimental result of the SRR. The green curve is simulated and the blue one is experimental. (b) Fitted dielectric constant from experimental result of SRR.

The transmission for all metamaterials is displayed in Fig. 3. Insets are optical microscope images of the fabricated metamaterials. The red curve indicates vertical electrical polarization and blue horizontal polarization, with respect to Fig. 1. Figure 3(a) is the transmission spectrum for the canonical SRR. The SRR transmission shows strong resonances at about 0.5, 1.5, and 2.3 THz. It is worth highlighting that the resonance strength is much higher than reported for SRRs on GaAs substrates; all the three resonances achieve values below 10%. Similar resonance strength also appears in Figs. 3(c) and 3(d); they both have strong resonances and are relatively broad-band. A comparison of the experimental and simulated transmission of the low frequency resonance of the SRR is shown in Fig. 4(a), and good agreement is evident. We also fitted the dielectric constant of SRR on parylene substrate shown in Fig. 4(b).

In conclusion, we designed, fabricated, and characterized several different metamaterials on parylene thin film substrates. Due to the low loss properties of parylene films, metamaterials exhibit strong electromagnetic response at THz frequencies. Coupled with the biostable and biocompatible properties of parylene film, our results indicate the potential future use of metamaterial/parylene composites for medical purposes, or other various applications.

Bibliography

[1] J. S. Song, S. Lee, S. H. Jung, G. C. Cha, and M. S. Mun, J. Appl. Polym. Sci. 112, 3677 2009.

[2] P. Hanefeld, U. Westedt, R. Wombacher, T. Kissel, A. Schaper, J. H. Wendorff, and A. Greiner, Biomacromolecules 7, 2086 2006.

[3] E. M. Schmidt, J. S. Mcintosh, and M. J. Bak, Med. Biol. Eng. Comput. 26, 96 1988.

[4] A. A Tracton, Coatings Technology Handbook CRC, 2008.

[5] D. C. Rodger, J. D. Weiland, M. S. Hamayun, and Y. C. Tai, Sens. Actuators B, 117, 107 2006.

[6] G. E. Loeb, M. J. Bak, M. Salcman, and E. M. Schmidt, IEEE Trans. Biomed. Eng. BME-24, 121 1977.

[7] F. A. Lindberg, IEEE Trans. Compon., Hybrids, Manuf. Technol., 14, 790 1991.

[8] S. Aoyagi, K. Furukawa, D. Ono, K. Ymashita, T. Tanaka, K. Inoue, and M. Okuyama, Sens. Actuators, A, 94, 145 2008.

[9] C. P. Tan, B. R. Seo, D. J. Brooks, E. M. Chandler, H. G. Craighead, and C. Fischbach, Integr. Comp. Biol., 1, 587 2009

[10] D. Devanathan and R. Carr, IEEE Trans. Biomed. Eng. BME-27, 671 1980.

[11] D. R. Smith, W. J. Padilla, D. C. Vier, S. C. Nemat-Nasser, and S. Schultz, Phys. Rev. Lett. 84, 4184 2000.

[12] J. B. Pendry, Phys. Rev. Lett. 85, 3966 2000.

[13] D. Schurig, J. J. Mock, B. J. Justice, S. A. Cummer, J. B. Pendry, A. F. Starr, and D. R. Smith, Science 314, 977 2006.

[14] N. I. Landy, S. Sajuyigbe, J. J. Mock, D. R. Smith, and W. J. Padilla, Phys. Rev. Lett. 100, 207402 2008.

[15] N. I. Landy, C. M. Bingham, T. Tyler, N. Jokerst, D. R. Smith, and W. J. Padilla, Phys. Rev. B 79, 125104 2009.

[16] M. Born and E. Wolf, Principles of Optics: Electromagnetic Theory of Propagation, Interference, and Diffraction of Light Cambridge University Press, Cambridge, 1999.

Chapter 7

Investigation of surface current modes for metamaterial with group theory method

7. 1 Introduction

Electromagnetic metamaterials, artificially engineered materials made from structured composites, have attracted increasing attention in the past decade. Metamaterials' abilities to achieve exotic properties that are difficult to attain with nature materials have been demonstrated. One such extraordinary property explored intensively early on in metamaterials research is negative refractive index which is theoretically predicted in 1968 [1] and experimentally demonstrated after 2000 [2, 3, 4]. Since then, research into metamaterials has grown enormously resulting in many novel phenomena including invisibility cloaks [5], perfect lenses [6, 7] and perfect absorbers [8, 9, 10, 11, and 12]

Although intensely studied, the response of metamateirals to electromagnetic wave is complicated and majority of the early studies have been focused on the primary resonant modes. There is a lack of suitable analytic method to systematically study the interaction between metamaterials and EM waves, particular for higher order resonant modes. metamaterials are normally composed of periodic structures which possess certain symmetry attributes and lattice distance of the periodic structures are much smaller than the wavelength they operate therefore could be described as effective medium[13]. Due

to the similarity in terms of symmetry properties between metamaterials and natural solid materials, it is intuitive to apply symmetry method to study the properties of metamaterials. Works utilizing group theory to study photonic crystals has been performed [14, 15] .Investigation of artificial metamaterials using group theory method was pioneered in [16].By using symmetric properties of metamaterials and their corresponding character table in point group theory, electromagnetic properties of metameterials such as bianisotropy and the tensor form of permittivity and permeability were determined.Those theoretical calculation agree well with experimental results. Recently metamaterials having unit cell contains multiple elements were investigated [17, 18] to obtain multi resonance. In [17] metamaterials unit cell in shape of checker board and honey cone were used and wallpaper group were assigned to these unit cells. Other work analyzing metamaterials using the same method for other various metamaterials also have been studies [19, 20, 21, and 22]. Isotropic three dimensional metamaterials was also investigated based on symmetry method [23].

In this work, we focus on investigating the resonant surface current modes for metamaterials, particular the first and second order modes, based on symmetry using group theory method. We are able to calculate the possible surface current modes for metamaterial with specific symmetry. We performed studies on two classical type of metamaterial structure and utilize computer simulations to verify our predictions.

7. 2 Symmetry and Surface Current Modes

Group theory is a well-established subject that has been used extensively to study the properties of solid state crystals and chemical molecular. By using symmetry property of a crystal or molecular, its intrinsic vibrational or rotational modes could be determined. Since metamaterials are normally composed of periodic structures that resembles an assemble of crystal or molecular with certain symmetry, we could make analogue between the electrical surface current modes of metamaterials to these vibrational mode and predict the surface current behavior using group theory method.

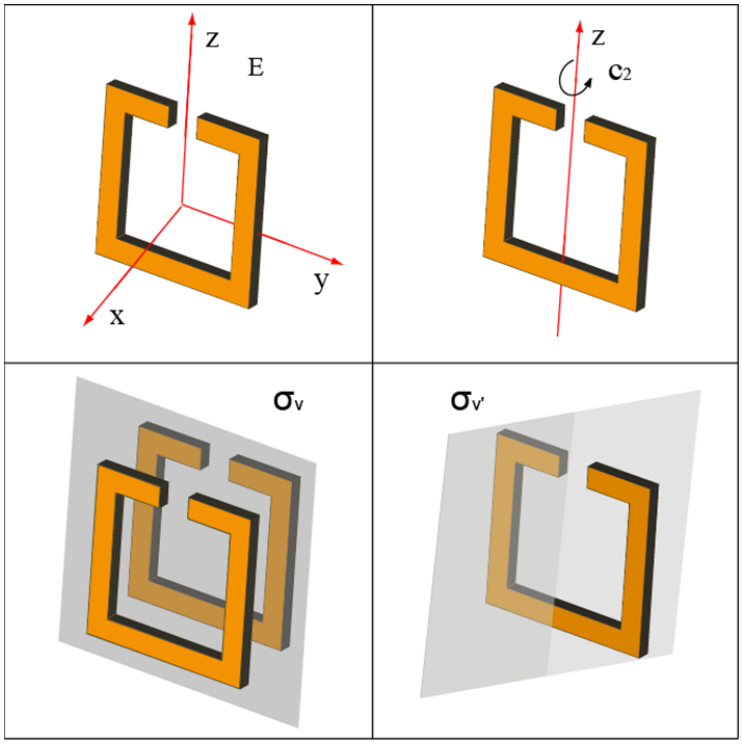

Fig. 1. Split Ring Resonator and the 4 symmetry elements it possess

When the electromagnetic wave come into interaction with metamaterials, surface current will be generated and the surface current oscillates long the structure with certain frequency. There will be infinite order of modes given that the EM wave spectra contain infinite high frequency. In practice, the primary and the first a few resonant modes is of more interests and can give a guide line of designing metamterials. However, at higher order resonant mode, the surface current behavior may be very complex and is difficult to be foreseen without a computer simulation. It will be beneficial for better understanding the metamaterials response mechanism if there is an analytical way to calculate the surface current before performing simulation or experiments. In this work, we present the

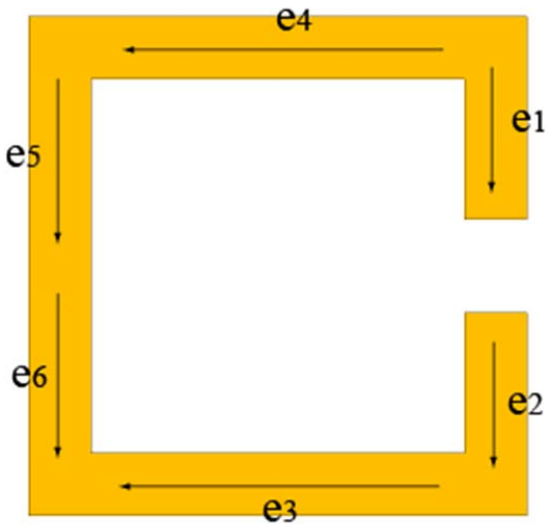

Fig. 2. Surface current basis set that assigned to the SRR

analysis of split ring resonator (SRR) and electric ring resonator (ERR) with point group theoretical methods to determine the possible surface current modes and we use computer simulation to verify the existence of the primary and second order modes.

Table 1. Character table of C_{2v} point group [24]

C_{2v}	E	C_2	σ_v	σ_v'	Linear	Quadratic
A_1	1	1	1	1	z	x^2,y^2,z^2
A_2	1	1	-1	-1	R_z	xy
B_1	1	-1	1	-1	x,R_y	xz
B_2	1	-1	-1	1	y,R_x	yz

7. 3 Study on split ring resonator

Surface current modes of the classical SRR was first studied. According to point group theory, the SRR structure belongs to the point group C_{2v} and it has four symmetry elements: identity operation E, a twofold axis of rotation C_2, two mirror planes σ_v and σ'_v as shown in Fig. 1. In group theory, each group has a corresponding character table which

Table 2. Effects of the basis set after applying the symmetry operation of the point group C_{2v}

	e_1	e_2	e_3	e_4	e_5	e_6	$\chi(g)$
E	e_1	e_2	e_3	e_4	e_5	e_6	6
C_2	$-e_2$	$-e_1$	e_4	e_3	$-e_6$	$-e_5$	0
σ_v	$-e_2$	$-e_1$	e_4	e_3	$-e_6$	$-e_5$	0
σ_v'	e_1	e_2	e_3	e_4	e_5	e_6	6

is two dimension table containing useful information of the group. The character table for C2v point group is shown as Table 1. The top left element of the table gives the name of the group. The first row is the symmetry operations and the first column is the irreducible representations (irrep) of the group.

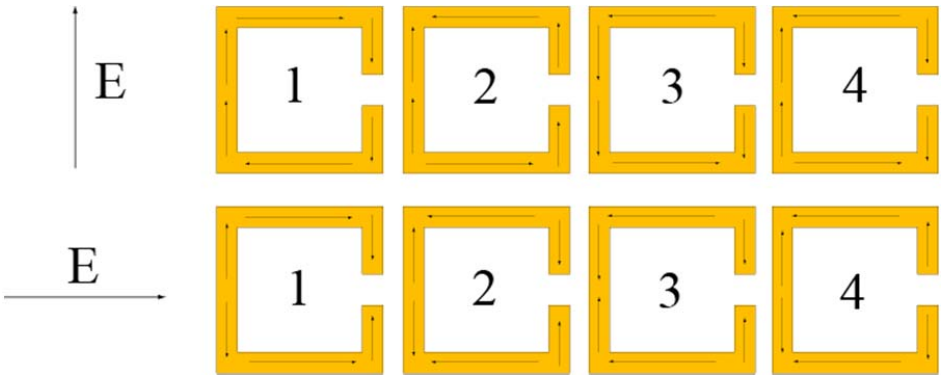

Fig. 3. Calculated possible surface current modes of the SRR for y and z polarized EM wave

When EM wave is incident on the SRR, surface current will be generated and oscillate along corresponding paths. Such response can be quite complicated, especially at higher order, i.e 2nd order resonance for complex structures with multiple sections. To include all possibilities and make comprehensive analysis, in this study, we first assign a basis set to the SRR which is a set of current vectors that indicate the possible surface current direction at each section of the SRR. The way we employ to assign the basis set is

Table 3. New sets of basis corresponding the 4 irreps of C_{2v} group

A_1	e_1-e_2	e_2-e_1	e_3+e_4	e_3+e_4	e_5-e_6	e_6-e_5	z
A_2	0	0	0	0	0	0	R_z
B_1	0	0	0	0	0	0	x,R_y
B_2	e_1+e_2	e_2+e_1	e_3-e_4	e_4-e_3	e_5-e_6	e_5+e_6	y,R_x

following: The bulk of the table lists the characters of the irreps under each symmetry operation. The last two column of the table give the various function that transform as the corresponding irreps. These functions are important in various application of group theory, such as spectroscopy [25].

- Treat the metamaterial as a two dimensional structure,ie no base vector is assigned along the direction perpendicular to the metamaterial surface.
- Each segment of the structure is given at least one base.
- For the segment that intersects with a reflection plane, assign basis to both sides of the segment that separated by the intersection plane.

Following these rules, we assign a basis of 6 base vectors (e_1, e_2, e_3, e_4, e_5, e_6) to the SRR structure which is shown in Fig.2. The directions of this basis are arbitrarily chosen to make the analysis valid in general circumstances. Then the SRR together with the assigned basis are transformed according to the four symmetry operations that belong to the C_{2v} point group: E, C2, σ_v and σ'_v. Meanwhile we trace the transformation of the six basis and record their directions and locations after the transformation. The transformation of the six bases under the operations is listed in Table 2. Then we can obtain the matrix representations for each element of the group with the following method.

- If the basis stays the same location and direction, give value 1.
- If the basis stays the same location but reverse direction, give value -1.
- Otherwise, give value0.

Adding the values in each row will give the character corresponding to each symmetry operation respectively. The reducible representation was computed and listed in the last column of Table 2. Then we can use a result of the Orthogonality Theorem to determine how many times each Irreducible Representation (irrep) occurs.The representation listed in the last column of Table 2 is a reducible representation and can be reduced to the irreps

of the point group. In order to do this, we make use of the Little Orthogonality Theorem (LOT):

$$a_m = \frac{1}{h}\sum_c n_c \chi(g)\chi_m(g) \tag{1}$$

where h is the order of the group, nc is the number of symmetry operations in class C, $\chi(g)$ is the character of new reducible representation, $\chi_m(g)$ is the character of irreps listed in the character table. By using the LOT, we found that the reducible representation of our basis is spanned by $3A_1+3B_2$. In the character table of C_{2v}, we see that in the column of linear function, A_1 corresponds to z and B_2 corresponds to y and R_x which means electrical field along z direction will generate A1 response and electrical field along y or magnetic field along x will generate B2 response.

After knowing the irreps spannned by the basis set, we then calculate the Symmetry Adapted Linear Combination (SALC) of our basis that transform the representative matrix of our original representation into block diagonal form. We use a projection operator to determine the symmetry adapted linear combinations that transforms as an irreducible representation which is given by:

$$\phi_i' = \sum_g \chi_k(g) g \phi_i \tag{2}$$

Where ϕ_i' is the SALC, $\chi_k(g)$ is the character of the k^{th} irrep, g is the symmetry operation, and ϕ_i is the basis function. Equation (3) can also be written as a matrix dot product:

$$\begin{pmatrix} \phi(A_1)' \\ \phi(A_2)' \\ \phi(B_1)' \\ \phi(B_2)' \end{pmatrix} = \begin{pmatrix} 1 & 1 & 1 & 1 \\ 1 & 1 & -1 & -1 \\ 1 & -1 & 1 & -1 \\ 1 & -1 & -1 & 1 \end{pmatrix} \times \begin{pmatrix} e1 & e2 & e3 & e4 & e5 & e6 \\ -e2 & -e1 & e4 & e3 & -e6 & -e5 \\ -e2 & -e1 & e4 & e3 & -e6 & -e5 \\ e1 & e2 & e3 & e4 & e5 & e6 \end{pmatrix} \tag{3}$$

The multiplication result for the SALC is shown as Table 3 where we ignore a constant 2 in front of it. We see in Table 3 only the row A_1 and B_2 have none zero values which means these two modes are active modes and the condition that which one is activated in listed in in the last column of Table 3: electrical field along z direction will generate A1 response and electrical field along y or magnetic field along x will generate B_2 response. In this study we only consider the electrical polarization condition.

The A_1 mode, according to the first row of Table 3, is an active mode if the electrical components of the EM wave is polarized along z direction, see Fig. 1. Note in Table 3, there is a new basis set containing 3 vectors (e_1-e_2, e_3+e_4, e_5-e_6) which are combination of our original 6 basis vectors. Here we treat the vectors with opposite sign as the same vector since since when oscillating the vector direction will change. For example e_5-e_6 and e_6-e_5 are treated as one vector. Using the three new base vectors, we predict that in the condition of x polarized EM wave:

- e_1 and e_2 will always point at different directions with respect to the direction we assign at the first place (both pointing downwards) therefore one of them will point up and the other one will point down. The same situation applies to e_5 and e_6. While e_3 and e_4 will always point at the same direction.
- Linear combination of the new vector set gives the entire possible surface current mode driven by the EM wave.

For the A1 mode there are therefore four predicted surface current modes as shown in the second column of Fig. 3. Similar analysis applies to the B2 mode as well and we predict four surface current modes as shown in the first column of Fig. 3. Among these

surface current modes, we will only focus on the primary and the second order modes and we use computer simulations to verify our predictions. CST microwave studio is used to simulated the electromagnetic response of the metamaterial and we use perfect electric and perfect magnetic boundary conditions to polarize the electric and magnetic field

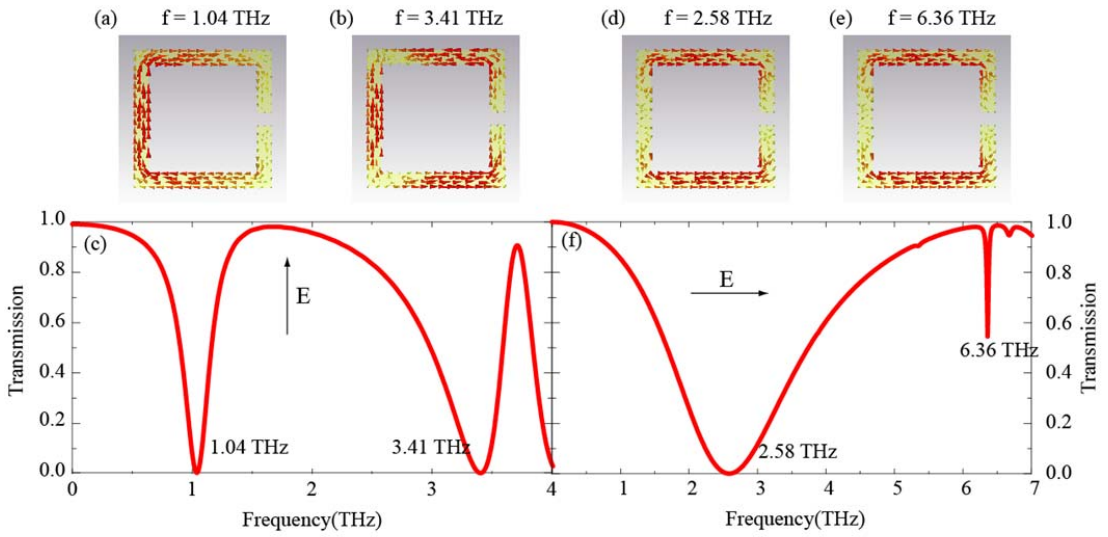

Fig. 4. (a) Simulated first order surface current for y polarization. (a) Simulated second order surface current for y polarization. (c) Simulated transmission for y polarization.(d) Simulated first order surface current for x polarization. (e) Simulated second order surface current for x polarization. (f) Simulated transmission for x polarization.

components, vertically and horizontally with respect to Figure 1. Waveguide ports were use on the remaining two boundaries to simulate a plane wave incident on the metamaterial. The transient solver is used to obtain the complex S parameters. We put surface current monitor at the resonance frequency positions the simulated surface current modes. Figure 4 displays the simulated transmission and first two orders surface

current modes of the SRR for the two polarized direction EM wave. Fig. a, b and Fig d, e shows the simulated surface current for the two cases in which the arrows denotes the direction of the surface current. The simulated surface current modes are well agreed as calculated using group theory method shown in Fig. 3.

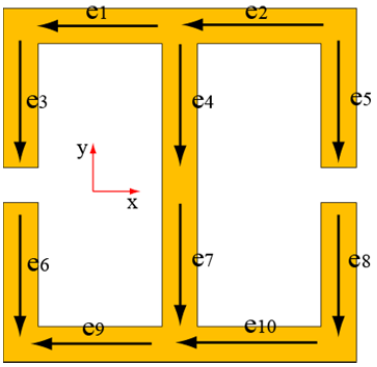

Fig. 5. Surface current basis set that assigned to the ERR

7. 4. Study on electric ring resonator

Table 4. Character table of D_{2h} point group

D_{2h}	E	C_z	C_y	C_x	i	σ_{xy}	σ_{xz}	σ_{yz}	linear rotations	quadratic
A_g	1	1	1	1	1	1	1	1		x^2,y^2,z^2
B_{1g}	1	1	-1	-1	1	1	-1	-1	R_z	xy
B_{2g}	1	-1	1	-1	1	-1	1	-1	R_y	xz
B_{3g}	1	-1	-1	1	1	-1	-1	1	R_x	yz
A_u	1	1	1	1	-1	-1	-1	-1		
B_{1u}	1	1	-1	-1	-1	-1	1	1	z	
B_{2u}	1	-1	1	-1	-1	1	-1	1	y	
B_{3u}	1	-1	-1	1	-1	1	1	-1	x	

To show the universality of our theory, we apply the group theory method on another classical metamaterial structure: ERR [26]. The ERR structure studied in this

section is shown in Figure 5. The ERR structures have eight symmetry elements E, C_2 (z), C_2(y), C_2(x), i, σ (xy), σ (xz), σ (yz) and belongs to D_{2h} point group. The character table for D_{2h} point group is shown as Table 4. Following the same rule in section 3, for the ERR structure, we assign ten base vectors with arbitrary direction as shown in Figure 5.

Analogue to the SRR analysis, Table 5 lists the transformation of the assigned basis under the symmetry elements of D_{2h} point. Similar calculation is performed according to Equation 3 and we are able to determine that the reducible representation for the ERR of our assigned basis is spanned by $3A_g+2B_{1g}+3B_{2u}+2B_{3u}$. The new vector basis for x and y polarized EM wave are [e1+e2+e9+e10), (e3+e8-e5-e6), e4=0, e7=0] and [(e1+e10-e2-e9), (e3+e8+e5+e6), (e4+e7)], correspondingly. The calculated surface current modes are listed in Figure 6 for both the x and y polarization. Figure 7 displays the simulated transmission and first two orders surface current modes of the ERR for the two polarized

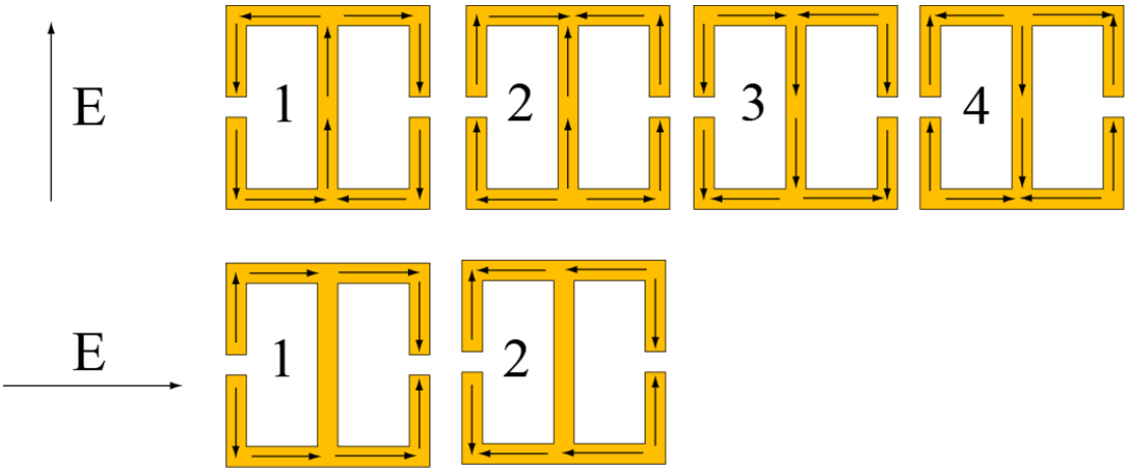

Fig. 6. Calculated surface current modes of the ERR for y and x polarization.

direction EM wave. Fig. a, b and Fig d, e shows the simulated surface current for the two cases in which the arrows denotes the direction of the surface current.

Table 5. Effects of the basis set after applying the symmetry operation of the point group D_{2h}

	e_1	e_2	e_3	e_4	e_5	e_6	e_7	e_8	e_9	e_{10}	$\chi(g)$
E	e_1	e_2	e_3	e_4	e_5	e_6	e_7	e_8	e_9	e_{10}	10
C_z	$-e_{10}$	$-e_9$	$-e_8$	$-e_7$	$-e_6$	$-e_5$	$-e_4$	$-e_3$	$-e_2$	$-e_1$	0
C_y	$-e_2$	$-e_1$	e_5	e_4	e_3	e_8	e_7	e_6	$-e_{10}$	$-e_9$	2
C_x	e_9	e_{10}	$-e_6$	$-e_7$	$-e_8$	$-e_3$	$-e_4$	$-e_5$	e_1	e_2	0
i	$-e_{10}$	$-e_9$	$-e_8$	$-e_7$	$-e_6$	$-e_5$	$-e_4$	$-e_3$	$-e_2$	$-e_1$	0
σ_{xy}	e_1	e_2	e_3	e_4	e_5	e_6	e_7	e_8	e_9	e_{10}	10
σ_{xz}	e_9	e_{10}	$-e_6$	$-e_7$	$-e_8$	$-e_3$	$-e_4$	$-e_5$	e_1	e_2	0
σ_{yz}	$-e_2$	$-e_1$	e_5	e_4	e_3	e_8	e_7	e_6	$-e_{10}$	$-e_9$	2

7. 5 Discussion and Conclusion

We have investigated surface current modes driven by EM wave for two different metamaterials structures with distinct symmetry properties using group theory method. The simulated surface current of the SRR and ERR metamaterials agree exactly with prediction for the first two order resonant modes. For both the SRR and ERR, there are some modes predicted by group theory cannot be found in simulation. Possible reasons for that are when going to higher frequency, the symmetry properties is broken and the structure does not act according to the corresponding group anymore.

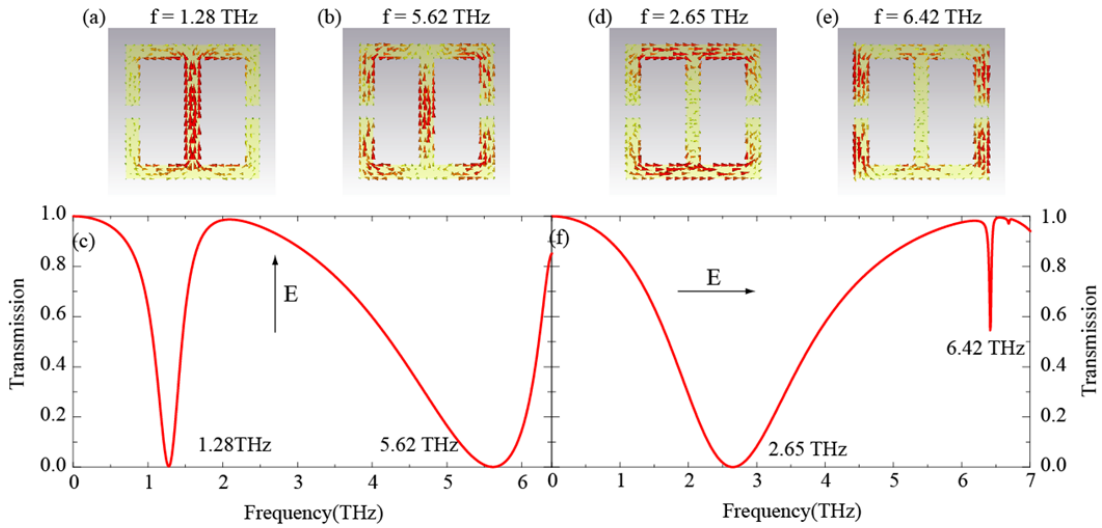

Fig. 7. a) Simulated first order surface current for y polarization. (a) Simulated second order surface current for y polarization. (c) Simulated transmission for y polarization.(d) Simulated first order surface current for x polarization. (e) Simulated second order surface current for x polarization. (f) Simulated transmission for x polarization.

In conclusion, surface current modes of two classical metamaterials structures are studies. Simulation results show that group theory method is a powerful way to study the electromagnetic properties of metamaterials. Future work may extend the method from point group theory to more general space group and we hope that this will open a door to study other important properties of metamaterials such as spatial dispersion.

Bibliography

[1]. V. G. Veselago,“The electrodynamics of substances with simultaneously negative values of e and m” Sov. Phys. Usp. 10, 509 (1968).

[2]. D. R. Smith,W. J. Padilla, D. C. Vier, S. C. Nemat-Nasser, and S. Schultz, “Composite Medium with Simultaneously Negative Permeability and Permittivity” Phys. Rev. Lett. 84, 4184–4187 (2000).

[3]. R. A. Shelby, D. R. Smith, and S. Schultz, “Experimental Verification of a Negative Index of Refraction” Science 292, 77 (2001).

[4]. D. R. Smith, J. B. Pendry and M. C. K. Wiltshire, “Metamaterials and Negative Refractive Index Science” 305, 788 (2004).

[5]. D. Schurig, J. J. Mock, B. J. Justice, S. A. Cummer, J. B. Pendry, A. F. Starr, and D. R. Smith, “Metamaterial Electromagnetic Cloak at Microwave Frequencies,” Phys. Rev. Lett. 314, 977-979 (2006).

[6]. J. B. Pendry,“Negative Refraction Makes a Perfect Lens” Phys. Rev. Lett. 85, 3966 (2000).

[7]. N. Fang, H. Lee, Ch. Sun, and X. Zhang, Science 308, 534 (2005).

[8]. N. I. Landy, S. Sajuyigbe, J. J. Mock, D. R. Smith, and W. J. Padilla, “Perfect Metamaterial Absorber,” Phys. Rev. Lett. 100,, 207402 (2008).

[9]. X. L. Liu, T. Starr, A. F. Starr, and W. J. Padilla, “Infrared Spatial and Frequency Selective Metamaterial with Near-Unity Absorbance” Phys. Rev. Lett. 104, 207403 (2010).

[10]. X. L. Liu, T. Tyler, T. Starr, A. F. Starr, N. M. Jokerst, and W. J. Padilla, “Taming the Blackbody with Infrared Metamaterials as Selective Thermal Emitters” Phys. Rev. Lett. 107, 045901 (2011).

[11]. J. M. Hao, J. Wang, X. L. Liu, W. J. Padilla, L. Zhou, and M. Qiu, “High performance optical absorber based on a plasmonic metamaterial,” Appl. Phys. Lett. 96, 251104 (2010).

[12]. N. Liu, M. Mesch, T. Weiss, M. Hentschel and H. Giessen, “Infrared Perfect Absorber and Its Application As Plasmonic Sensor,” Nano Lett. 10, 2342 (2010).

[13]. D. R. Smith, S. Schultz, P. Markos and C. M. Soukoulis, “Determination of effective permittivity and permeability of metamaterials from reflection and transmission coefficients,” Phys. Rev. B. 65, 195104 (2002).

[14]. V. Dmitriev, “Symmetry properties of 2D magnetic photonic crystals with square lattice,” Eur. Phys. J. Appl. Phys. 32, 159–165 (2005).

[15]. V. Dmitriev, “Face-centered cubic magnetic photonic crystals: Some general electromagnetic properties followed from symmetry,” Metamaterials 2, 71–76 (2008).

[16]. W. J. Padilla, ”Group theoretical description of artificial electromagnetic metamaterials, Opt. Express 15,, 1639- 1664 (2006).

[17]. C. M. Bingham, H. Tao, X. Liu, R. D. Averitt, X. Zhang, andW. J. Padilla, “Planar wallpaper group metamaterials for novel terahertz applications,” Optics Express 16, 18565-18575 (2008)

[18]. Y. Yuan, C. Bingham, T. Tyler, S. Palit, T. H. Hand,W. J. Padilla, D. R. Smith, N. M. Jokerst, and S. A. Cummer, “Dual-band planar electric metamaterial in the terahertz regime,” Opt. Express 16, 9746–9752 (2008).

[19]. O. Isik, and K. P. Esselle, “Analysis of spiral metamaterials by use of group theory,” Metamaterials 3, 33–43 (2009)

[20]. N.Wongkasemand, A. Akyurtlu, and K. A. Marx, “Group theory based design of isotropic negative index metamtaterials,” Progress In Electromagnetics Research 63, 295–310 (2006)

[21]. K. Matra and N. Wongkasem, “Left-handed chiral isotropic metamaterials: analysis and detailed numerical study,” J. Opt. A: Pure Appl. Opt. 11, 074011 (2009)

[22]. C. M. Reinke, Teofilo M. De la Mata Luque, M. F. Su, M. B. Sinclair, and Ihab El-Kady, “Group-theory approach to tailored electromagnetic properties of metamaterials: An inverse-problem solution,” Phys. Rev. E 83, 066603 (2011)

[23]. J. D. Baena, L. Jelinek, and R. Marqus, “Towards a systematic design of isotropic bulk magnetic metamaterials using the cubic point groups of symmetry,” Physical Review B 76, 245115 (2007)

[24]. M.S. Dresselhaus, G. Dresselhaus, and A. Jorio “Group Theory: Application to the physics of Condensed Matter”Springer (2008).

[25]. D.C. Harris and M.D. Bertoluccu “SYMMETRY AND SPECTROSCOPY: An Introduction to Vibrational and Electronic Spectroscopy” Dover (1978).

[26]. W. J. Padilla, et al., “Electrically resonant terahertz metamaterials: Theoretical and experimental investigations,” Physical Review B Rapids 75, 041102R (2007).